REPORT DOCUMENTATION PAGE

Form Approved
OMB No. 0704-0188

1a. REPORT SECURITY CLASSIFICATION	1b. RESTRICTIVE MARKINGS
UNCLASSIFIED	

DTIC
ELECTE
OCT 3 1 1988
R(S)
D

AD-A201 481

3. DISTRIBUTION/AVAILABILITY OF REPORT

Approved for Public Release;
Distribution Unlimited

5. MONITORING ORGANIZATION REPORT NUMBER(S)

AFOSR-TR- 88-1164

6a. NAME OF PERFORMING ORGANIZATION	6b. OFFICE SYMBOL (If applicable)	7a. NAME OF MONITORING ORGANIZATION
UNIVERSITY OF KENTUCKY		AFOSR/NA

6c. ADDRESS (City, State, and ZIP Code)	7b. ADDRESS (City, State, and ZIP Code)
DEPT. OF CIVIL ENGINEERING LEXINGTON, KY 40506-0046	Bldg. 410 Bolling AFB, DC 20332-6448

8a. NAME OF FUNDING/SPONSORING ORGANIZATION	8b. OFFICE SYMBOL (If applicable)	9 PROCUREMENT INSTRUMENT IDENTIFICATION NUMBER
AFOSR	NA	AFOSR-84-0195

8c. ADDRESS (City, State, and ZIP Code)

Bldg. 410
Bolling AFB, DC 20332-6448

10. SOURCE OF FUNDING NUMBERS

PROGRAM ELEMENT NO.	PROJECT NO.	TASK NO	WORK UNIT ACCESSION NO.
6.1102F	2302	C1	

11. TITLE (Include Security Classification)   (U)

THREE-DIMENSIONAL ELASTO-PLASTIC ANALYSIS FOR SOILS (UNCLASSIFIED)

12. PERSONAL AUTHOR(S)
HARDIN, B. O. AND BLANDFORD, G. E.

13a. TYPE OF REPORT	13b. TIME COVERED	14. DATE OF REPORT (Year, Month, Day)	15. PAGE COUNT
FINAL	FROM 6/15/84 TO 8/14/88	October 15, 1988	83

16. SUPPLEMENTARY NOTATION

17. COSATI CODES			18. SUBJECT TERMS (Continue on reverse if necessary and identify by block number)
FIELD	GROUP	SUB-GROUP	ELASTO-PLASTIC NONLINEAR THREE-DIMENSIONAL
			FINITE ELEMENT SOILS

19. ABSTRACT (Continue on reverse if necessary and identify by block number)

This report presents the U.S. Air Force Office of Scientific Research contract (Project No. AFOSR-84-0195) accomplishments in perfecting the elasto-plastic constitutive equations of Hardin (1978) and their implementation into EPSAP (Elasto-Plastic Soil Analysis Program). Essential features of soil behavior that result from the soil skeleton being particulate are included in the soil model. It is recognized that the plastic behavior of particulate materials depends on direction of the effective stress increment as well as state of effective stress. Two classes of stress increment directions are defined with different plastic potential and hardening functions for each class.

Specific research considered during the contract period has dealt with: (1) crushing of soil particles; (2) modeling soil strength in terms of effective stress; (3) modifications of the Class 1 plastic potential function; (4) modeling work softening behavior for Class 1 plastic hardening; (5) formulation of a model for triaxial compression

20. DISTRIBUTION/AVAILABILITY OF ABSTRACT	21. ABSTRACT SECURITY CLASSIFICATION
☒ UNCLASSIFIED/UNLIMITED ☐ SAME AS RPT. ☐ DTIC USERS	UNCLASSIFIED

22a. NAME OF RESPONSIBLE INDIVIDUAL	22b. TELEPHONE (Include Area Code)	22c. OFFICE SYMBOL
Major Steven C. Boyce	(202) 767-6963	AFOSR/NA

DD Form 1473, JUN 86   Previous editions are obsolete.   SECURITY CLASSIFICATION OF THIS PAGE

UNCLASSIFIED

88

19.   Continued

of soils including the construction and analysis of the database; (6) development of the theory and basis for defining Class 1 hardening in terms of triaxial compression; (7) modeling Class 2 plastic hardening; (8) formulation of models for one-dimensional strain in soils including the construction and analysis of the database; (9) development of the theory and basis for defining Class 2 hardening in terms of 1D-strain; (10) development of objective elastic soil constitutive equations which include stress history, particle deposition, fabric anisotropy, and stress state; (11) development and numerous enhancements of a three-dimensional elasto-plastic finite element soil analysis program based on the developed constitutive equations; (12) low-stress dilation testing; (13) the effect of rigid boundaries on the measurement of particle concentration; and (14) initiation of work aimed toward the development of a computer simulation of the behavior of three-dimensional packings of nonspherical particles.

THREE-DIMENSIONAL ELASTO-PLASTIC ANALYSIS FOR SOILS

By

Bobby O. Hardin

and

George E. Blandford

Department of Civil Engineering
University of Kentucky
Lexington, KY 40506-0046

Accesion For

NTIS CRA&I	☑	
DTIC TAB	☐	
Unannounced	☐	
Justification		

By

Distribution /

Availability Codes

	Avail and/or	
Dist	Special	
A-1		

DTIC COPY INSPECTED 4

October 3, 1988

THREE-DIMENSIONAL ELASTO-PLASTIC ANALYSIS FOR SOILS

TABLE OF CONTENTS

INTRODUCTION

In recent years, studies in soil dynamics have dealt extensively with wave propagation in soils. Both laboratory and field wave velocities have been measured in an effort to determine the various parameters that affect wave propagation. Wave propagation is an excellent technique for applying extremely small strains to soils and to accurately measure the stress-strain response of the soils due to the small strains. Such small strains are nearly elastic. Consequently, studies of wave propagation in soil dynamics have contributed greatly to the understanding of elastic soil behavior.

However, due to the use of limiting equilibrium analyses in soil statics, studies in soil statics have tended to concentrate on the strength of soils and on large strain behavior. Large strains involve slippage, rearrangement, and crushing of particles. These are sources of plastic strain. The studies of plastic strains in soil statics have led to the use of work hardening plasticity theories in soil mechanics, the development of critical state soil mechanics, and to the development of stress-dilatancy theory (Drucker, et al. 1957; Rowe, 1962; and Schofield and Wroth, 1968).

Hardin (1978) presented a state-of-the-art paper on the stress-strain behavior of soils in which information on the elastic behavior of soils from soil dynamics is synthesized with information on the plastic behavior of soils from soil statics. Synthesizing these two types of soil behavior provided a framework for the development of comprehensive elasto-plastic stress-strain relationships for soils. The stress-strain relations are formulated in terms of effective stress and particulate mechanics is used as a guide for the development of macroscopic constitutive equations. In particular, the Hertz and Mindlin (1949) theories have to do with the elastic behavior of soils and the stress-dilatancy theory is related to the plastic behavior of soils (Rowe, 1971).

Many constitutive equations currently being proposed for soils arise from studies in continuum mechanics. They are often carefully constructed from the continuum mechanics point of view, but show little regard for the constraints imposed by particulate mechanics, i.e. the

1

kinematics of particle movement, particle crushing, and the bonding at particle contacts. As a result, the physical meaning of the coefficients in the constitutive equations is often obscure, and a given set of values for the coefficients is valid for a very restricted range of loading.

To provide physically based elasto-plastic soil constitutive equations, the U. S. Air Force Office of Scientific Research has sponsored the research summarized in this report through its Project No. AFOSR-84-0195. The overall project objective is the development and verification of three-dimensional elasto-plastic constitutive equations for soils. Essential features of soil behavior that result from the soil skeleton being particulate are included and the developed soil model incorporates the behavior characteristics indicated by particulate mechanics theories. The construction of the elastic component of the constitutive equations is influenced by the Hertz and Mindlin theories. The plastic component is formulated using the stress-dilatancy theory and includes the dependency of particulate materials on the effective stress increment direction as well as state of effective stress. This is accounted for by defining two plasticity models for two respective classes of stress increment directions with different plastic potential and hardening functions for each class.

Because the developed constitutive equations have been constructed by synthesizing small strain data from soil dynamics with data for large strains from soil statics (Hardin, 1978), a given set of coefficients is valid for a wide range of loading conditions, from wave propagation strain levels to loadings where the soil fails. The constitutive equations include such state and stress history parameters as void ratio and overconsolidation ratio. Consequently, some of the effects of changes in these parameters are accounted for directly and therefore do not cause variations in the coefficients. Many of the coefficients are nearly constant for a wide variety of soils and loading conditions, and the effects of soil disturbance on some of the coefficients is beginning to be understood.

This report focuses on the developed elasto-plastic constitutive equations and their implementation into a three-dimensional finite element code EPSAP (Elasto-Plastic Soil Analysis Program). The deve-

2

loped constitutive equations are based on assuming the soil to be a continuum. This is necessary in order to obtain solutions to practical geotechnical engineering problems. However, one should always remember that the soil is composed of discontinuous particles and the properties of the coninuum should reflect the essential features of soil behavior that result from the particulate nature of soils. Primary emphasis of this project has been on the understanding and realistic modeling of the constitutive behavior of soils. The finite element program has been developed for use in the verification of the constitutive model; but can also be used for the analysis of three-dimensional soil systems.

At the beginning of the project in 1984, the principal investigators believed that the constitutive equations by Hardin (1978) could be perfected and implemented into a three-dimensional finite element analysis program in a relatively short time. It would then be possible to solve boundary value problems corresponding to laboratory tests, e.g. the vertical loading of model footings on sands. However, the ideas for improvement of constitutive models that have been discovered during the project were unforseen and the complexity of numerical implementation was underestimated. Consequently, as the project concludes, the analysis program is just now ready for solution of problems involving monotonic loading of cohesionless soils. The development of constitutive equations for cohesive soils and cyclic loading has been advanced but requires considerable additional effort. Thus, the verification of constitutive equations has been by comparison to test results for specimens subjected to homogenous states of stress and strain. Verification by finite element simulation of footing tests, etc., has not been completed.

A complete set of constitutive equations and numerical procedure for the monotonic load analysis of cohesionless soils are presented herein and will be submitted for publication in the near future. Though the focus is on the final stage of the supported research effort, some of the other accomplishments previously reported are summarized. A brief overview and summary of the published results for the project are presented in the next section.

3

PROJECT OVERVIEW AND PUBLICATION SUMMARIES

Three-dimensional elasto-plastic constitutive equations for soils are comprised of the elemental parts listed in Table 1. Much of the framework in Table 1 and preliminary definition of many of the elemental parts was presented by Hardin (1978). Research completed under the current contract has aimed primarily toward improved definition of the plastic potential surfaces and work hardening and softening functions for monotonic loading. An important development discovered during the past year is the implicit definition of plastic potential surfaces. Principal plastic strain increment ratio functions representing the gradients of plastic potential functions are defined. This provides flexibility in defining surface shapes that accurately model soil behavior and simplifies numerical evaluation of the plastic strain increments.

Details of accomplishments have been reported to AFOSR in project reports and through copies of papers published or submitted for publication. The items studied are listed in Table 2 with references to appropriate papers or reports containing results. A brief summary of each paper submitted for publication is included below in chronological order.

Soil Particle Crushing (Hardin, 1985a). - The strength and stress-strain behavior of an element of soil is affected greatly by the degree to which particle crushing or particle breakage takes place during loading and deformation. For the type of deformation that primarily produces volume change, such as one-dimensional strain or isotropic compression (Class 2 stress increments), particle crushing adds to the reduction in volume. For the type of deformation where particles are moving past or around one another, such as triaxial compression or simple shear (Class 1 stress increments), crushing at sliding contacts decreases the rate of dilation corresponding to a given principal stress ratio.

In order to understand the physics of the strength and stress-strain behavior of soils and to devise mathematical models that adequately represent such behavior, it is important to define the degree to which the particles of an element of soil are crushed. The amount of particle crushing that occurs in an element of soil under stress depends

4

Table 1.— ELEMENTAL PARTS OF 3D CONSTITUTIVE EQUATIONS

EFFECTS OF SOIL DISTURBANCE AND AGING	
* ELASTIC COMPONENT (Hertzian)	
* PLASTIC COMPONENT	
DEFINITION OF LOADING	
For Monotonic Loading	
Class 1	Class 2
PLASTIC POTENTIAL SURFACE	PLASTIC POTENTIAL SURFACE
WORK HARDENING AND SOFTENING FUNCTION	WORK HARDENING FUNCTION
For Cyclic Loading	
Class 1	Class 2
YIELD RATE SURFACE	PRECONSOLIDATION SURFACE
MASING	UNLOAD—RELOAD SHAPE
KINEMATIC HARDENING	KINEMATIC HARDENING
ANISOTROPY (PACKING AND STRESS) ROTATION OF STRESS INCREMENT	
* VISCOUS COMPONENT (Strain Rate Effects)	

5

Table 2 - Research Accomplishments

Constitutive Behavior

Task	Papers, Reports and Comments
Soil Elasticity	Hardin, B. O. and Blandford, G. E. (1988a), "Elasticity of Particulate Materials," submitted to Journal of Geotechnical Engineering: draft submitted to AFOSR.
Particle Crushing	Hardin, B. O. (1985), "Crushing of Soil Particles," Journal of Geotechnical Engineering, ASCE, Vol. 111, No. 10, pp. 1177-1192.
Strength of Soils	Hardin, B. O. (1985), "Strength of Soils in Terms of Effective Stress," Proceedings of the Richart Commemorative Lectures, ASCE, Detroit, October, pp. 1-78.
	Hardin, B. O. (1988b), "The Low-Stress Dilation Test," accepted for publication in the Journal of Geotechnical Engineering, ASCE: draft submitted to AFOSR.
Class 1 Plastic Potential Surface	"Class 1 Plastic Potential Function Formulation Appendix III, first annual report to AFOSR, Sep. 26, 1985.
	Class 2 Plastic Potential: Modification of the Class 1 plastic Surface potential function also applies to Class 2,because the Class 1 function is a component of the Class 2 function.
Class 1 Work Hardening and Softening Function	"Modeling Work Softening Behavior for Class 1 Plastic Hardening," Appendix II, second annual report to AFOSR, Sep. 15, 1986.
	Hardin (1988d), "Triaxial Compression for Cohesionless Soils," to be submitted to Journal of Geotechnical Engineering, ASCE.

Table 2 - Research Accomplishments (continued)

Task	Papers, Reports and Comments
Class 1 Work Hardening and Softening Function (continued)	A database which contains several hundred stress-strain curves from drained triaxial compression tests has been completed.
Class 2 Work Hardening Function	"Modeling Class 2 Plastic Hardening," Appendix III, second annual report to AFOSR, Sep. 15, 1986.
	Hardin (1987), "1D Strain in Normally Consolidated Cohesionless Soils," Journal of Geotechnical Engineering, ASCE, Vol. 113, No. 12, pp. 1449 - 1467.
	Hardin (1988a), "1D Strain in Normally Consolidated Cohesive Soils," Journal of Geotechnical Engineering, ASCE, 39 pp., to be published.
Application	Hardin, et al. (1988), "Triaxial Compression, Simple Shear, and Strength of Wheat, International Summer Meeting of the ASAE, Rapid City, SD, June 26-28, 1988, Paper #88-4022; in review for possible publication in the Transactions of the ASAE.

Finite Element Analysis

Task	Papers, Reports and Comments
Matrix Formulation of Constitutive Equations	"Matrix Formulation of Constitutive Equations," section of first annual report to AFOSR, Sep. 26, 1985, pp. 8-13.
3D Constitutive Equations	Hardin and Blandford (1988b), "3D Constitutive Equations for Cohesionless Soils," to be submitted to Journal of Geotechnical Engineering, ASCE.
Implementation of Constitutive Equations into Finite Element Code	Because the constitutive equations are being developed and revised, the finite element code must be continuously updated to include newly developed models.

7

Table 2 - Research Accomplishments (continued)

Task	Papers, Reports and Comments
Development of Three-Dimensional Element Library	"Finite Element Formulation Details," Appendix V, second annual report to AFOSR, Sep. 15, 1986. (includes representation of infinite boundaries); plus this report.
Investigation of Nonlinear Solution Strategies	"Nonlinear Solution Algorithm," section of second annual report to AFOSR, Sep. 15, 1986, pp. 16-22; and this report.
Finite Element Code Verification	A soil specimen subjected to homogeneous states of stress along a specified stress path is represented using one modified hexahedron finite element for the symmetric one-eighth of the problem. The computed stress-strain relation is compared to that computed directly from the constitutive equations.
	Some results of the finite element part of this verification procedure are given in "Verification Problems," section of second annual report to AFOSR, Sep. 15, 1986, pp. 22-27; and this report.
3D Elasto-Plastic Finite Element Analysis	Blandford and Hardin (1988), "3D Elasto-Plastic Finite Element Analysis of Cohesionless Soils," to be submitted to International Journal for Numerical and Analytical Methods in Geomechanics.

on particle size distribution, particle shape, effective stress state, effective stress path, void ratio, particle hardness (i.e. hardness of cementing material or weakest constituent of a particle and weakest particles of an element), and the presence or absence of water.

Data for a large number of single mineral soils and rockfill-like materials have been analyzed and equations developed that can be used to estimate the total breakage expected for a given soil subjected to a given loading. In doing this, new measures of particle breakage have been defined, called breakage potential, total breakage, and relative breakage, that integrate the changes in the particle size distribution curve for all sizes greater than 0.074 mm. A methodology based on probability analysis for studying the breakage of particles of each size within a distribution of sizes has been outlined. Continued development of the probability model for particle crushing is currently supported by the National Science Foundation.

Soil Strength in Terms of Effective Stress (Hardin, 1985b). - An understanding of the strength of soils is essential to the formulation of general-purpose constitutive models for soils. Failure is a limiting case and should be defined first, so that the form of equations adopted for various elements of the constitutive model (the Class 1 hardening function in particular) will behave properly as limiting conditions are approached. The Mohr-Coulomb failure theory is used by most geotechical engineers to model the strength of soils. However, a more fundamental approach that considers the particulate nature of soils has been pursued.

Factors that determine soil strength (e.g. confinement, density, particle size distribution, mineral friction, aging, particle crushing, etc.) produce their effect through their influence on two fundamental mechanisms of resistance to deformation in particulate materials. These two fundamental mechanisms are

* bonding at particle contacts, and

* the kinematics of particle movement within an element of deforming soil.

The first of these fundamental mechanisms is physio-chemical in nature and the second is geometric. Inclusion of these two basic mechanisms must be considered in determining the appropriate soil strength model. Figure 1 illustrates the developed strength model. The two parameters that represent the two basic mechanisms of soil strength are the bonding obliquity angle ϕ_o and the maximum rate of dilation d_{max}. Variation of these parameters with minor principal stress σ_3' is illustrated in Figs. 1(b) and 1(c) and the resulting strength envelope is shown on the Mohr diagram in Fig. 1(a). The maximum rate of dilation curve is defined directly from the results of strength tests (normally triaxial compression); whereas the strength model must be used to determine the bonding obliquity angle from the same tests. Curvature of the strength envelope in Fig. 1(a) results from variation with stress of the two fundamental parameters ϕ_o and d_{max}.

The bonding obliquity angle is equal to the mineral friction angle for cohesionless soils, but includes cohesive and frictional bonding for cohesive materials. A method for isolating the magnitudes of cohesive and frictional bonding in cohesive materials is proposed. Analysis of triaxial compression test results for stabilized sands shows that the dimensionless contact cohesion parameter is a measure of the strength of cementation bonding.

The model is generalized with respect to stress path through the dilatancy factor and the interpolation function F(b) (refer to the paper for precise definition of these terms). The dilatancy factor ties together the values of maximum rate of dilation for different stress paths. Experiments indicate that the dilatancy factor is independent of stress path for a given material at a given density. The interpolation function accounts for the effect of stress path on energy transmission and dissipation at the peak principal stress ratio. The interpolation function F(b) may be chosen to give identical or differing strengths in triaxial compression and extension. It can also be chosen so that the value of $b = (\sigma_2' - \sigma_3')/(\sigma_1' - \sigma_3')$ for plane strain matches test results.

Model calibration has been performed using the results of over 700 triaxial compression tests, most on cohesionless materials. The analyzed database includes silts, uniform and well graded sands, and rockfill-like materials with maximum particle sizes up to 200 mm, as
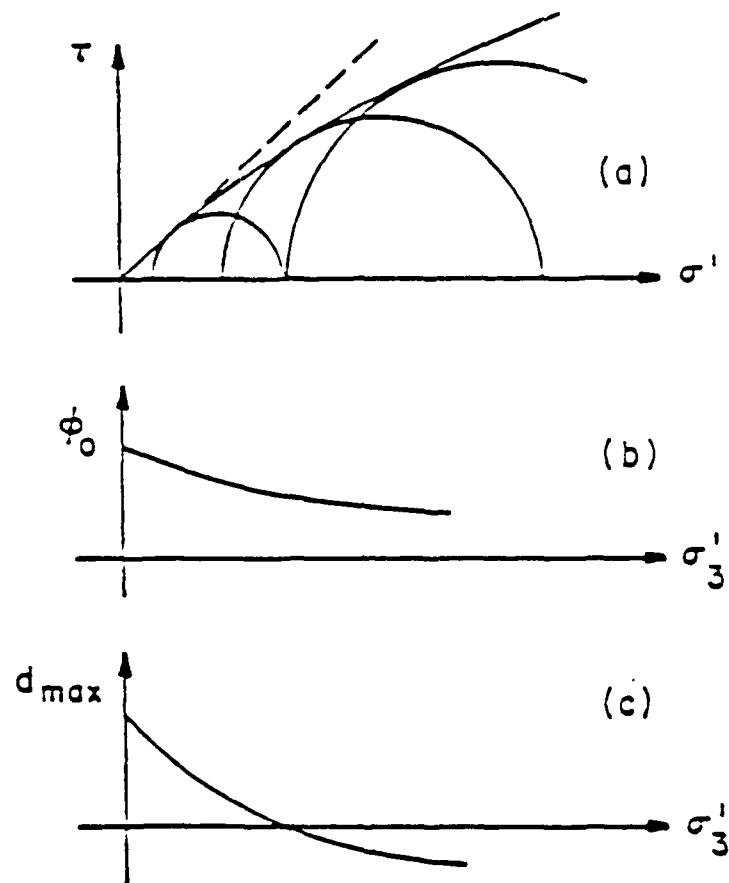
Fig. 1. Strength Model

well as normally and heavily overconsolidated clays and stabilized sands. Cohesionless materials range in hardness from chlorite and calcite to aluminum oxide, with particle shapes from round to angular. The minor principal stress varies from 0.01 to 677 atmospheres, with an overall void ratio range from 0.17 to 1.28.

An example is presented in the paper showing how the model may be used to estimate the strength of materials that cannot be tested. Thus, the model may prove useful to engineers involved in the design of large earth and rockfill structures.

One-Dimensional Strain in Soils (Hardin, 1987; 1988a). - The first paper compares a stress-strain model for one-dimensional strain in normally consolidated cohesionless soils to test results covering the stress range 0 to 1300 atmospheres. This model is called the "$1/e$ vs. $\sigma_v'^p$ model" because the implied relationship between void ratio e and vertical effective stress σ_v' is linear in the low-stress range. The relationship between $1/e$ and $\sigma_v'^p$ is nonlinear at higher stresses where the effect of particle crushing becomes significant. Effects of initial void ratio, relative density, particle shape, particle size distribution, and particle material on 1D-strain behavior have been examined in the framework of the model. The model can accurately represent 1D-strain in rockfill-like materials as well as sands and gravels. The data and equations presented provide a means of estimating shrinkage during placement of rockfills and estimating settlement of structures on rockfills where it is not practical to conduct 1D-strain tests or penetration tests.

The second paper compares a stress-strain model for one-dimensional strain in normally consolidated cohesive soils to test results covering the stress range 0 to 950 atmospheres. For cohesive soils the $1/e$ vs. $\sigma_v'^p$ relationship is linear in the normally consolidated range. The slope of the linear relationship is nearly independent of soil disturbance and its variation is relatively small for a wide variety of soils with different compressibilities. Because of this the effects of aging and soil disturbance are isolated to a single model parameter, providing a quantative measure of these effects. The liquid limit is easily related to the model because the $\sigma_v' = 0$ state is included. These

12

features provide for better interpretation of test results. An undisturbed sample can be tested as usual and then remolded to a water content slightly above the liquid limit. The liquid limit should be measured as water is added and the soil remolded. The final remolded sample should then be subjected to a 1D strain test. Results for both undisturbed and remolded samples define the model slope and the liquid limit and remolded test results are beneficial in choosing the best value of p. By following this procedure all three tests are conducted on identical material.

The one-dimensional strain models for normally consolidated soils are used to define Class 2 plastic hardening for monotonic loading (see Table 1). In order to define Class 2 plastic hardening for cyclic loading the unload-reload shape for 1D-strain must be modeled. This introduces additional complexity because the $1/e$ vs. $\sigma_v'^p$ relationship for unload-reload is nonlinear, the shape of the unload-reload curve depends on stress history as represented by the preconsolidation stress, and the preconsolidation stress is just one point on a preconsolidation surface when we generalize to three-dimensions.

Application of Constitutive Models to Wheat (Hardin, et al., 1988). - Some aspects of constitutive behavior are common to all particulate materials, e.g. the importance of bonding at particle contacts and the dilatancy of dense particulate materials. Thus, constitutive equations developed for cohesionless soils can often be applied to wheat with relatively little modifications provided the material constants are measured for wheat.

Hardin, et al. (1988) utilize models developed for soils to define the constitutive behavior of bulk wheat. Two models define three-dimensional behavior: a model for wheat elasticity (small-strain behavior) and a model for the strength of wheat. An elasto-plastic model for the behavior of wheat in triaxial compression is presented. The model includes the volume change behavior during triaxial compression and is in that sense three-dimensional. Simple shear and triaxial compression behaviors are compared by normalizing the two moduli versus strain relationships.

13

Low Stress Dilation Testing (Hardin, 1988b; to be published). - The low-stress dilation test is a new test; used in conjunction with other tests to define the peak strength of a particulate material. It provides a measure of kinematics of particle movement within a deforming element of particles making its results fundamental to the definition of soil strength and to the modeling of triaxial compression in soil. The low-stress dilation test relates to the geometric component of soil strength.

The objective of the test is to measure the rate of dilation in a particulate specimen deforming with minor principal stress $\sigma_3' = 0$. Initially, the test was referred to as an "unconfined" dilation test. However, in order to maintain necessary contact between specimen and apparatus the value of σ_3' must be somewhat greater than zero; leading to the name "low-stress" dilation test.

Dilation refers to the volume changes that occur during deformation of a particulate material. The relationship between volumetric and major principal strains during triaxial compression or plane strain loading is illustrated schematically in Fig. 2. Rate of dilation d, as measured by the test, is the rate at which volumetric strain v changes with major principal strain ϵ_1 (d $= -dv/d\epsilon_1$). The rate of dilation in Fig. 2 changes continuously with increasing ϵ_1, first increasing to the maximum value d_{max}, then decreasing to zero as the strain becomes very large.

Maximum rate of dilation increases with decreasing confinement. The maximum value of d_{max} at $\sigma_3' = 0$ is denoted $d_{o\sigma}$ (Fig. 2). The low-stress dilation test has been conceived as a simple means of measuring $d_{o\sigma}$.

Parameter $d_{o\sigma}$ is one of the coefficients in a strength model proposed by Hardin (1985b). The nature of the model is illustrated in Fig. 3 where it is applied to peak strength of a cohesionless rockfill-like material measured by four drained triaxial compression tests. Two model parameters represent the two basic mechanisms of soil strength. They are the bonding obliquity angle ϕ_o, which for cohesionless soils is equal to the mineral friction angle ϕ_μ (Fig. 3b), and the maximum rate of dilation d_{max} (Fig. 3c). Both ϕ_μ and d_{max} vary with σ_3' as shown in Fig. 3, with maximum values occurring at $\sigma_3' = 0$ ($\phi_{\mu o\sigma} = 39.8°$ and $d_{o\sigma} =$
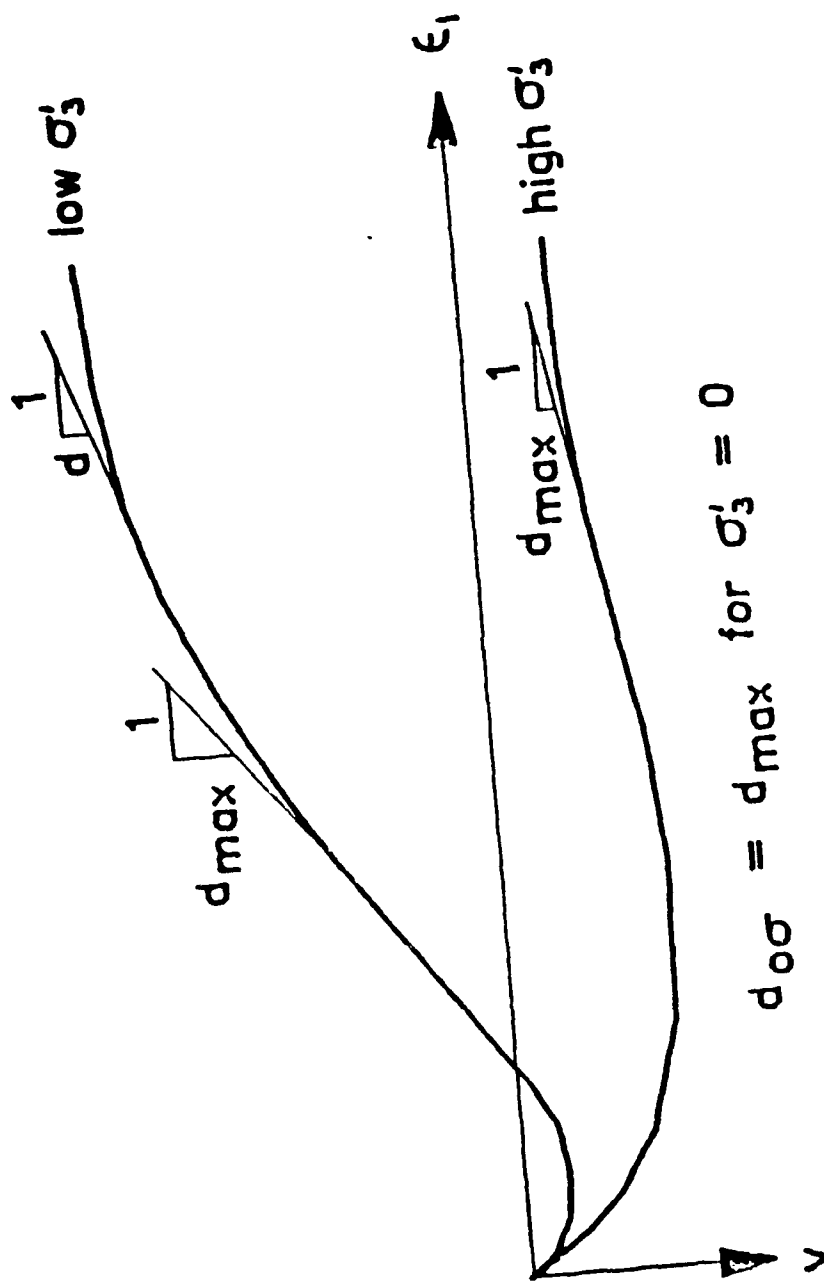
14

Fig.2. Definitions: rate of dilation, d; maximum rate of dilation, d_{max}; and maximum rate of dilation for $\sigma_3' = 0$, $d_{o\sigma}$
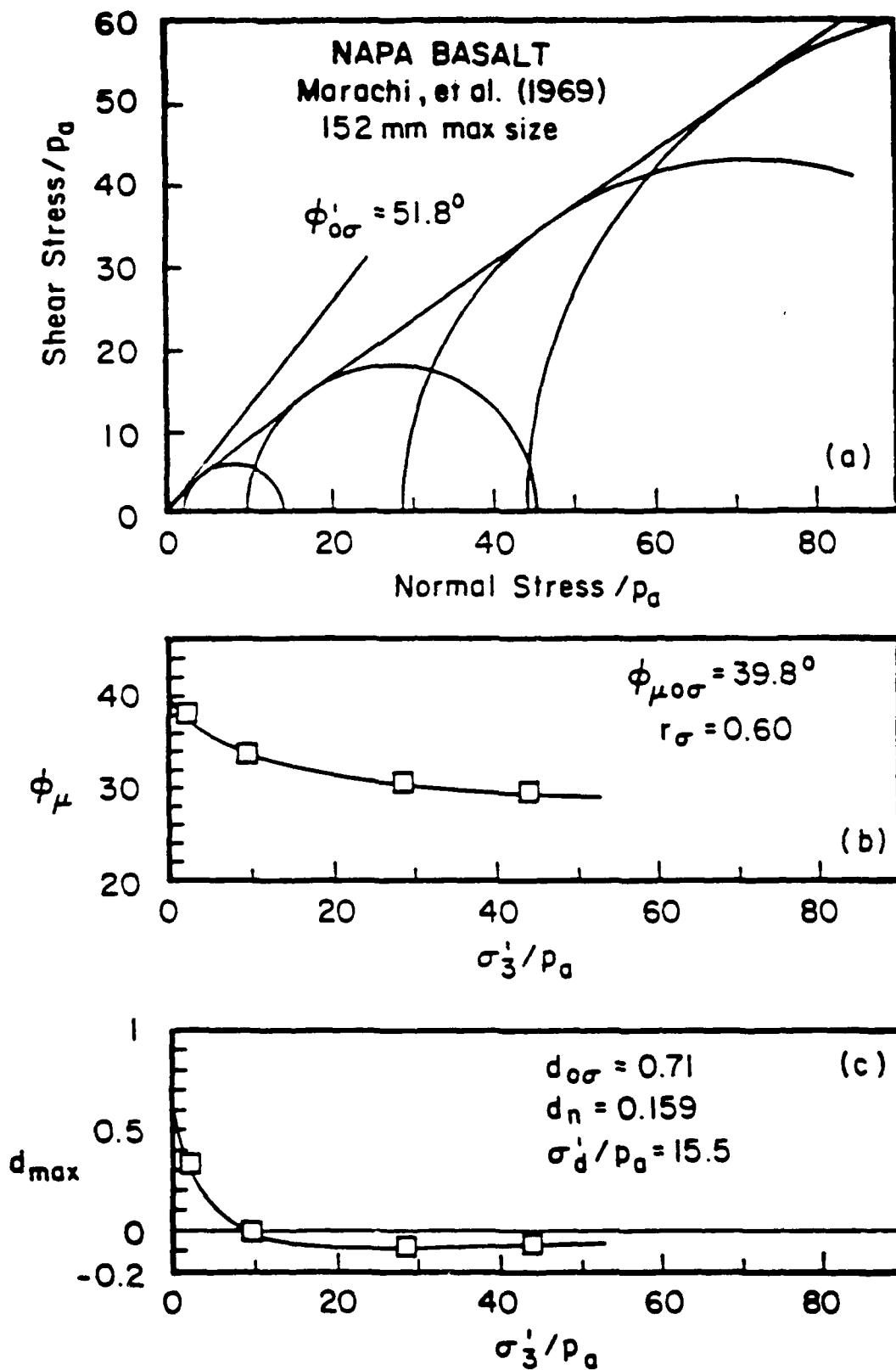
Fig. 3. Strength Model and Test Results for Napa Basalt

16

0.71, respectively). The curved Mohr envelope defined by the ϕ_μ and d_{max} variations is compared to the measured Mohr circles in Fig. 3(a). Derivation of the strength model and discussion of its application to cohesive soils can be found in Hardin (1985b).

The test apparatus described in this paper is relatively small in size, designed to test sands. However, an important feature of the low-stress dilation test is its potential for testing rockfill-like materials. It should be relatively easy (compared to large-scale triaxial compression testing) to construct a low-stress dilation apparatus that could test 1 to 2 m^3 specimens.

This paper includes discussion of the strength model, description of the test apparatus and procedure, and a theoretical analysis and test results for a packing of brass rods. Data for Ottawa sand, crushed quartz sand, and a graded sand are analyzed to develop a model for the effect of initial void ratio on low-stress dilation behavior of cohesionless materials; and critical state behavior is discussed. Test results showing the effect of fabric anisotropy on dilation behavior are presented and a test on sand-cement indicates the role of contact cohesion in the physics of soil strength.

Measurement of Particle Concentration (Hardin, 1988c; in review). - Particle concentration is a physical property of particulate materials that has great influence on their mechanical behavior. Void ratio or porosity are the parameters most often used to quantify particle concentration. The determination of void ratio or porosity of a soil sample is part of the procedure for many ASTM standards.

Soil samples are often formed by placement in a mold with rigid boundaries, followed by striking off a plane surface with a rigid straightedge. Such rigid boundaries and plane surfaces interrupt the packing of particles. When the volume of the sample is computed from the volume of the rigid mold and plane surfaces, additional void space at the boundaries that is not representative of the void ratio or porosity of a repeating element of the packing is included in the volume. The computed void ratio or porosity are too large and the error increases with decreasing sample size.

This paper describes the results of theoretical and experimental

studies of the effect of rigid boundaries on void ratio or porosity measurement. An equation is presented that relates the true void ratio to measured void ratio, accounting for mold size and shape, and particle size distribution. The relationship is shown to be nearly independent of particle shape and true density.

Elasticity of Particulate Materials (Hardin and Blandford, 1988a; in review). - A major difficulty in formulating elastic constitutive equations for materials composed of discrete solid particles is that the stress-strain behavior is rarely exclusively elastic. Deformation of a particulate material almost always involves slippage at contacts between particles as well as elastic deformation of individual particles. Elastic deformation is relatively small and is often obscured by plastic deformation resulting from slippage, rearrangement and crushing of particles. The problem is to isolate, measure and model the elastic behavior of particulate materials in the presence of pervasive yielding.

The elastic behavior of classical elasto-plastic materials is isolated by unloading; stress paths inside the yield surface are assumed to produce elastic strains. But particulate materials yield during unloading; consequently, exclusively elastic behavior is restricted to infinitesimal increments of unloading. Therefore, differential elastic constitutive equations for particulate materials are formulated using measurements of elastic stiffness for specimens subjected to a variety of ambient states of stress.

Previously, Hardin (1978) developed three-dimensional elastic differential constitutive equations for soils. However, these equations (including modifications by Hardin 1980) were not formulated to assure objectivity. The primary purpose of the reformulation presented in the paper is to satisfy objectivity. Another purpose is to incorporate the discovery by Roesler (1979) that elastic shear stiffness is independent of the stress normal to the plane of shear.

There are at least two important uses for the proposed elastic constitutive equations. They may be used to define the elastic strain increment for incremental elasto-plastic analysis; accurate definition of elastic strains is important since they are necessary for inverting the elasto-plastic stress-strain relations. Secondly, the equations

provide a three-dimensional framework for defining the effects of state of stress and soil density on wave propagation velocities. The equations for various elastic moduli (shear modulus, constrained modulus, etc.) are all defined by the three-dimensional equations.

Papers in Preparation - Three papers are currently being pursued for possible publication. The three papers are tentatively titled: "Triaxial Compression for Cohesionless Soils" by Hardin (1988d), "3D Constitutive Equations for Cohesionless Soils" by Hardin and Blandford (1988b), and " 3D Elasto-Plastic Finite Element Analysis for Cohesionless Soils" by Blandford and Hardin (1988). A brief description of each of these three papers is presented in the paragraphs below. Upon completion of the papers, copies will be sent to the AFOSR.

Triaxial compression for cohesionless soils (Hardin, 1988d) presents the formulation and verification of a model for the stress-strain behavior of cohesionless soils in triaxial compression. The model includes work softening and accurately represents the volumetric strain behavior. Results of hundreds of drained triaxial compression tests with volume change measurements available in the literature have been incorporated into a computerized database. These test results have been used to formulate the model. The developed 3D constitutive equations use the triaxial compression model to define the Class 1 hardening function.

Use of a triaxial compression model to simulate results for six tests on a crushed calcite sand is illustrated in Fig. 4. The six samples range from loose to dense with initial relative densities D_{ri} = 0.21 to 0.72, initial void ratios e_i = 0.661 to 1.027 and σ_3'/p_a = 2.04 for all tests. The measured variations of principal stress ratio and volumetric strain with axial strain are shown in Figs. 4a and 4b and the corresponding curves computed from the model are given in Figs. 4c and 4d.

The paper "3D Constitutive Equations for Cohesionless Soils" by Hardin and Blandford (1988b) presents the mathematical formulation of a complete model for monotonic loading of cohesionless soils. The objective is to present a complete constitutive equation algorithm that can be incorporated into finite element analysis programs with minimum
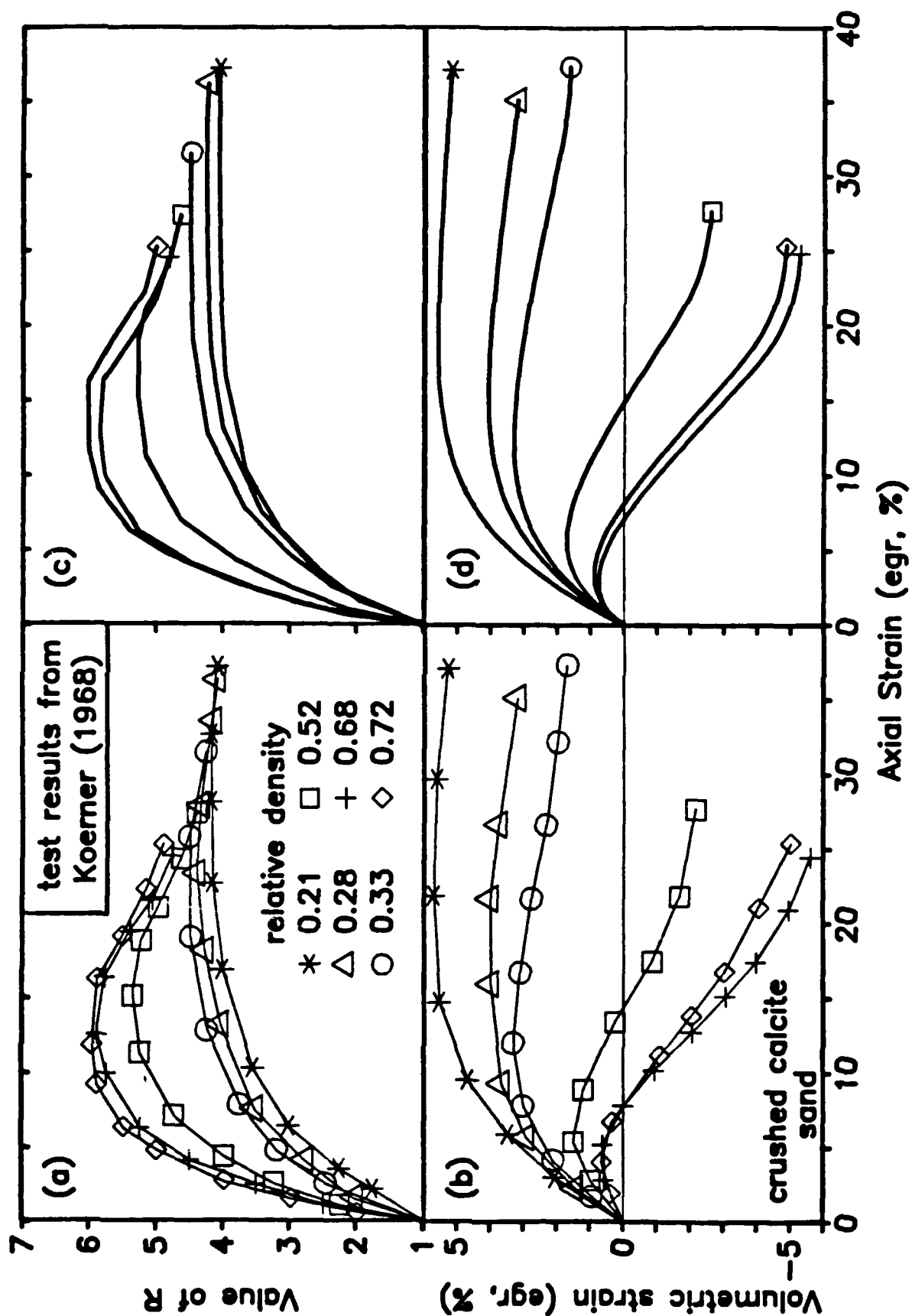
19

Fig.4. Test Results and Triaxial Compression Model for Crushed Calcite

20

effort. The paper includes many of the equations presented in the "Soil Elasticity" and "Soil Plasticity" sections of this report. However, the equations are arranged in the order and format necessary for computation.

Blandford and Hardin (1988) present a three-dimensional finite element implementation for the constitutive equations of Hardin and Blandford (1988a, b). Included in this effort is an initial stress solution algorithm for solving the nonlinear algebraic equations based on a second-order predictor-corrector scheme. Computational details associated with calculating the void ratio, load step scaling at the break point between pre-peak and post-peak (work softening behavior) Class 1 behavior and the variable load path algorithm are presented. Sample experimental problems are simulated demonstrating the correctness of the finite element implementation and the results for a plane strain footing problem (boundary value problem) are also presented.

THREE-DIMENSIONAL ELASTO-PLASTIC COHESIONLESS SOIL ANALYSIS

This portion of the report presents the current elasto-plastic constitutive equations and their implementation into a three-dimensional finite element code EPSAP (Elasto-Plastic Soil Analysis Program). The elasto-plastic constitutive equations are being investigated for publication (Hardin, 1988d; Hardin and Blandford, 1988b and Blandford and Hardin, 1988). However, the equations have been sufficiently developed to pursue their implementation into EPSAP as well as perform some numerical experiments.

EPSAP has been developed to solve three-dimensional cohesionless soil problems based on natural (true) stress-strain elastic and plastic constitutive equations presented in Hardin and Blandford (1988a,b). EPSAP includes a linear line element (Fig. 5a) to model line traction loads, a four node quadrilateral surface traction load element (Fig. 5b), the modified eight node hexahedron volume element of Wilson et al. (1973) including the patch test modifications of Taylor et al. (1976) (Fig. 5c) and an infinite element from Marques and Owen (1984) which is based on the mapping technique of Zienkiewicz et al. (1981, 1983) (Fig. 5d). Solution of the incremental elasto-plastic finite element equations is based on an initial stress formulation which utilizes a
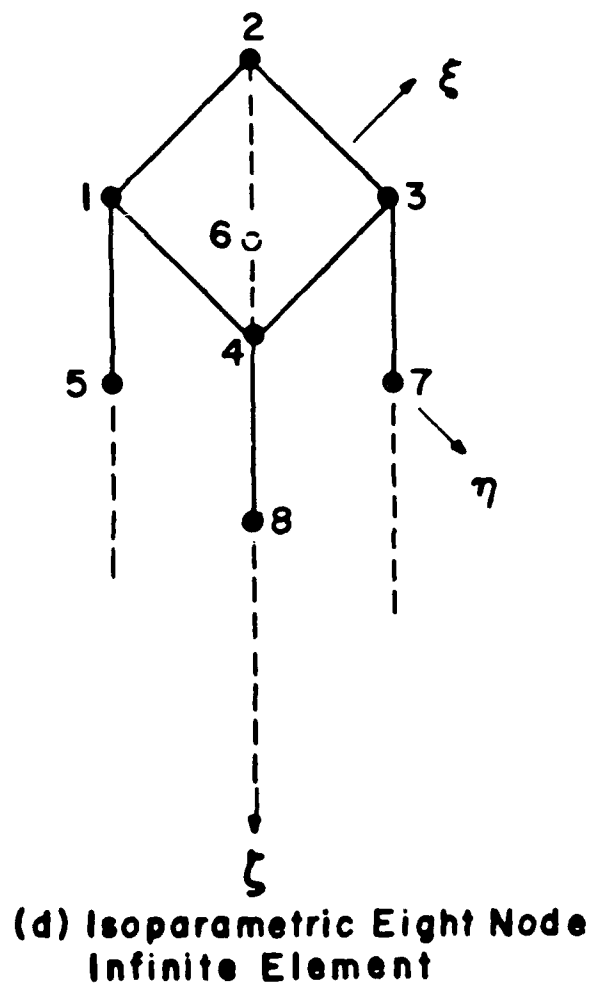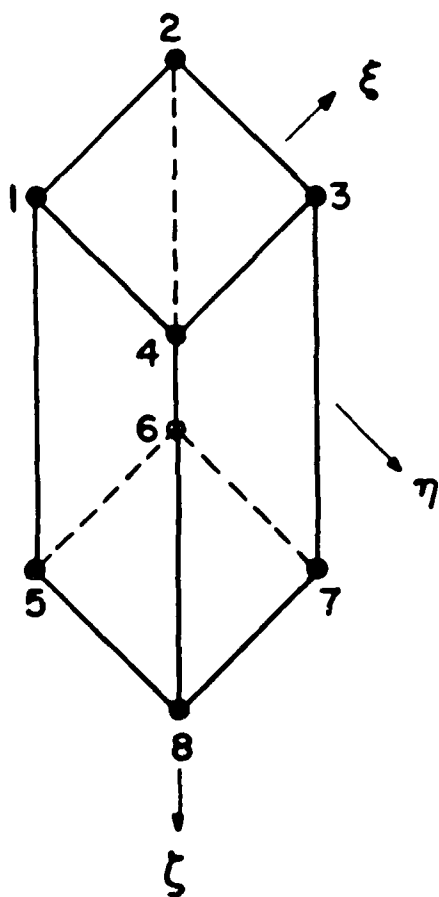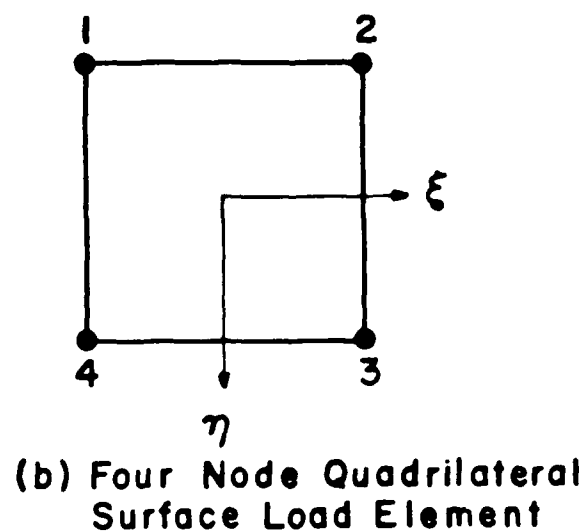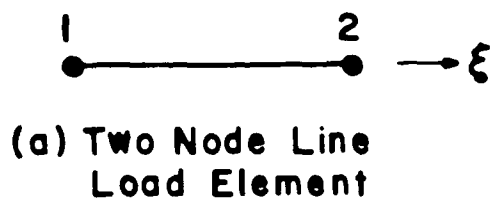
(a) Two Node Line
Load Element

(b) Four Node Quadrilateral
Surface Load Element

(c) Modified Eight Node
Hexahedron Element

(d) Isoparametric Eight Node
Infinite Element

Fig. 5. Finite Element Library

22

predictor-midpoint iterative corrector scheme to satisfy equilibrium. A natural (true) stress and strain finite element representation is obtained by updating the nodal coordinates during the analysis (Hsu, 1986). These items are discussed in the following sections along with some of the details for implementing the elastic and plastic constitutive models and the presentation of some standard numerical procedure verification problems.

SOIL ELASTICITY

Hardin and Blandford (1988a) concluded that elasticity modeling for particulate materials needs to include: (1) geometry of the assemblage (fabric); (2) elastic properties of individual particles; (3) stress history; and (4) current state of stress. These effects were included in the developed constitutive equations by a scaler function and three matrices representing different parts of the constitutive behavior for cohesionless soils, i.e.

$$\{d\epsilon^e\} = \frac{F(e)}{p_a^{1-n}} [S_\nu] [S_f] [S_\sigma] \{d\sigma'\}$$

$$= [S] \{d\sigma'\} \tag{1}$$

where $F(e) = 0.3 + 0.7e^2$ approximates the effect of void ratio e which changes with subsequent stress history; p_a is atmospheric pressure; n is a power stress coefficient; $\{d\epsilon^e\} = \lfloor d\epsilon_x^e \ d\epsilon_y^e \ d\epsilon_z^e \ d\gamma_{xy}^e \ d\gamma_{yz}^e \ d\gamma_{zx}^e \rfloor^T$ is the incremental elastic strain vector; $\{d\sigma'\} = \lfloor d\sigma_x' \ d\sigma_y' \ d\sigma_z' \ d\tau_{xy} \ d\tau_{yz} \ d\tau_{zx} \rfloor^T$ is the effective incremental stress vector; $[S_\nu]$ is the isotropic elastic Poisson ratio matrix (Table 3); $[S_f]$ is the reference soil fabric matrix (Table 4) which is defined to account for fabric geometry, elastic particle properties, and stress history prior to measurement of reference fabric; $[S_\sigma] = [R_\sigma]^{-1} [\Sigma] [R_\sigma]$ is the transformed stress-compliance matrix (Table 5) which is used to model the effect of state of stress on the constitutive coefficients including changes in soil fabric that result from stress history following the measurement of reference fabric (i.e. stress history effects not accounted for by $F(e)$); [S] is the nonlinear elastic material compliance matrix; { }

Table 3. Isotropic Elastic Poisson Ratio Matrix $[S_\nu]$

$$[S_\nu] = \begin{bmatrix} 1 & -\nu & -\nu & & & \\ -\nu & 1 & -\nu & & & \\ -\nu & -\nu & 1 & & & \\ & & & 2(1+\nu) & & \\ & & & & 2(1+\nu) & \\ & & & & & 2(1+\nu) \end{bmatrix}$$

Table 4. Reference Soil Fabric Matrix $[S_f]$
(x,y,z - Principal Fabric Directions)

$$[S_f] = \begin{bmatrix} \dfrac{1}{S_x} & & & & & \\ & \dfrac{1}{S_y} & & & & \\ & & \dfrac{1}{S_z} & & & \\ & & & \dfrac{1}{S_{xy}} & & \\ & & & & \dfrac{1}{S_{yz}} & \\ & & & & & \dfrac{1}{S_{zx}} \end{bmatrix}$$

Table 5. Stress Compliance Matrices ($[S_\sigma] = [R_\sigma]^{-1} [\Sigma] [R_\sigma]$)
($\sigma_1 \geq \sigma_2 \geq \sigma_3$; Principal Stresses)

$$[\Sigma] = \begin{bmatrix} \dfrac{1}{\sigma_1'^{\,n}} & & & & & \\ & \dfrac{1}{\sigma_2'^{\,n}} & & & & \\ & & \dfrac{1}{\sigma_3'^{\,n}} & & & \\ & & & \dfrac{1}{(\sigma_1'\sigma_2')^{n/2}} & & \\ & & & & \dfrac{1}{(\sigma_2'\sigma_3')^{n/2}} & \\ & & & & & \dfrac{1}{(\sigma_3'\sigma_1')^{n/2}} \end{bmatrix}$$

24

Table 5. Continued

$[R] =$

$$\begin{bmatrix} \ell_1^2 & m_1^2 & n_1^2 & 2\ell_1 m_1 & 2m_1 n_1 & 2n_1 \ell_1 \\ \ell_2^2 & m_2^2 & n_2^2 & 2\ell_2 m_2 & 2m_2 n_2 & 2n_2 \ell_2 \\ \ell_3^2 & m_3^2 & n_3^2 & 2\ell_3 m_3 & 2m_3 n_3 & 2n_3 \ell_3 \\ 2\ell_1 \ell_2 & 2m_1 m_2 & 2n_1 n_2 & 2(\ell_1 m_2 + \ell_2 m_1) & 2(m_1 n_2 + m_2 n_1) & 2(n_1 \ell_2 + n_2 \ell_1) \\ 2\ell_2 \ell_3 & 2m_2 m_3 & 2n_2 n_3 & 2(\ell_2 m_3 + \ell_3 m_2) & 2(m_2 n_3 + m_3 n_2) & 2(n_2 \ell_3 + n_3 \ell_2) \\ 2\ell_3 \ell_1 & 2m_3 m_1 & 2n_3 n_1 & 2(\ell_3 m_1 + \ell_1 m_3) & 2(m_3 n_1 + m_1 n_3) & 2(n_3 \ell_1 + n_1 \ell_3) \end{bmatrix}$$

$$[R_\epsilon] = [R] \, [\hat{I}]$$

$$[R_\epsilon]^{-1} = [R]^T \, [\hat{I}]$$

$$[R_\sigma] = [\hat{I}] \, [R]$$

$$[R_\sigma]^{-1} = [\hat{I}] \, [R]^T$$

$$\hat{I} = \text{diag} \begin{bmatrix} 1 & 1 & 1 & \frac{1}{2} & \frac{1}{2} & \frac{1}{2} \end{bmatrix}$$

ℓ_i, m_i, n_i - principal stress direction cosines

symbolize column vector; ⌊ ⌋ represent row vector; [ ] is used to designate a matrix; and superscript T denotes matrix transpose. Stress invariants (Table 6) have been used in formulating the stress-compliance matrix, in order to make the resulting strain-stress relation independent of coordinate transformation (objective).

SOIL PLASTICITY

There are important differences between classical plasticity and soil plasticity. In classical plasticity the direction of the plastic strain increment vector is assumed to depend on the state of stress but is considered independent of the stress increment vector direction. This is not the case for soils, as can be illustrated by considering the strain increments resulting from triaxial compression (TC) and isotropic compression (IC) stress increments. Figure 6(a) shows these two principal stress increments added to an initial isotropic state of stress. Figure 6(b) shows the resulting principal strain increments. The two strain increment vectors do not coincide. Hence the direction of the strain increment vector is not uniquely determined by the state of effective stress. This peculiar behavior of soils arises due to the particulate composition of soil materials. Soil stress-strain behavior is controlled to a great extent by the kinematics of particle movement.

Hardin (1978) shows that the elements required to define soil plasticity are

* a definition of loading,

* plastic potential functions for the different classes of loading, and

* hardening functions for the classes of loading.

The definition of loading is used to specify different classes of loading for different stress increment vector directions, and to specify whether a given stress increment constitutes loading or unloading. Hence, the definition of loading and plastic potential functions define those aspects of the model that are usually defined by the yield function in classical plasticity.

Hardin (1978) concluded that the behavior of soils can be represented, with sufficient accuracy for most purposes, by considering only

26

Table 6. Stress Invariants

$$I_1 = \sigma'_x + \sigma'_y + \sigma'_z$$

$$J_2 = \frac{1}{6} \left[(\sigma'_x - \sigma'_y)^2 + (\sigma'_y - \sigma'_z)^2 + (\sigma'_z - \sigma'_x)^2 \right]$$
$$+ \tau^2_{xy} + \tau^2_{yz} + \tau^2_{zx}$$

$$J_3 = (\sigma'_x - \sigma'_m)(\sigma'_y - \sigma'_m)(\sigma'_z - \sigma'_m) + 2\,\tau_{xy}\,\tau_{yz}\,\tau_{zx}$$
$$- (\sigma'_x - \sigma'_m)\tau^2_{yz} - (\sigma'_y - \sigma'_m)\tau^2_{zx} - (\sigma'_z - \sigma'_m)\tau^2_{xy}$$

$$\sigma'_m = I_1/3$$

$$\sigma'_i = \frac{1}{3}\left[I_1 + \beta_i(\theta)\, J_2^{1/2} \right] \quad ; \quad i = 1, 2, 3$$

$$\beta_1 = \sqrt{3}\,\sin\theta + 3\cos\theta$$

$$\beta_2 = -2\sqrt{3}\,\sin\theta$$

$$\beta_3 = \sqrt{3}\,\sin\theta - 3\cos\theta$$

$$\sin 3\theta = \frac{3\sqrt{3}\,J_3}{2\,J_2^{3/2}}$$

$$-\pi/6 \leq \theta \leq \pi/6$$

27

two fundamental classes of loading. These two classes are called Class 1 and Class 2 loadings. The deviatoric component of stress has the major influence on the deformation resulting from Class 1 loading, whereas the isotropic component of stress is more significant for Class 2 loading. A stress increment may be exclusively Class 1 or Class 2, or it may involve a combination of the two. Separation of the two classes of behavior is based on particle kinematics (not strictly deviatoric versus isotropic components). Class 1 stress increments produce the type of particle kinematics to which stress-dilatancy is applicable. Stress-dilatancy theory is used to define the Class 1 plastic potential function. Stress-dilatancy theory is not directly applicable to Class 2 loadings. Consequently, two plastic potential functions and two hardening functions, corresponding to the two classes of loading, are needed to define the plastic strains in soils.

The plastic strain increments, $d\epsilon^P_{ij}$, for each class of loading can be represented as

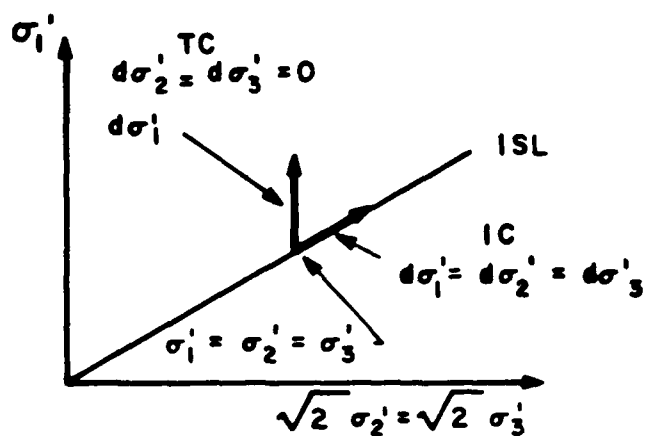$$(d\epsilon^P_{ij})_k = d\lambda^h_k \frac{\partial g_k}{\partial \sigma'_{ij}} \tag{2}$$

where $d\lambda^h_1$ and $d\lambda^h_2$ are the incremental hardening functions for Class 1 and Class 2 loadings, respectively; g_1, g_2 represent the Class 1 and Class 2 plastic potential functions (e.g. Fig. 7); and σ'_{ij} are the effective stress components. The total plastic strain increment is defined as

$$d\epsilon^P_{ij} = (1 - \psi) (d\epsilon^P_{ij})_1 + \psi (d\epsilon^P_{ij})_2 \tag{3}$$
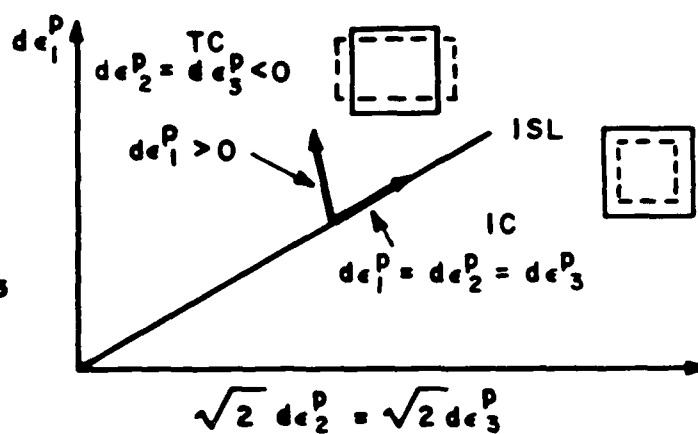
The values of ψ (which represents the level of class participation) are given in Fig. 8 for different stress increment paths from the state of effective stress defined by point A. Figure 8 constitutes the loading definition.

A simplified explanation of the difference between the behaviors for Class 1 and Class 2 stress increments is that Class 1 stress increments (e.g. triaxial compression, plane strain compression and simple shear) approach the strength envelope (failure); whereas, Class 2

28

σ_1'

TC
$d\sigma_2' = d\sigma_3' = 0$

$d\sigma_1'$

ISL

IC
$d\sigma_1' = d\sigma_2' = d\sigma_3'$

$\sigma_1' = \sigma_2' = \sigma_3'$

$\sqrt{2}\,\sigma_2' = \sqrt{2}\,\sigma_3'$

(a) Stress Increments

$d\epsilon_1^p$

TC
$d\epsilon_2^p = d\epsilon_3^p < 0$

$d\epsilon_1^p > 0$

ISL

IC
$d\epsilon_1^p = d\epsilon_2^p = d\epsilon_3^p$

$\sqrt{2}\,d\epsilon_2^p = \sqrt{2}\,d\epsilon_3^p$

(b) Plastic Strain Increments

Fig. 6. Comparison of Plastic Strain Increments for TC (Triaxial Compression) and IC (Isotropic Compression; ISL - Isotropic Stress Line)
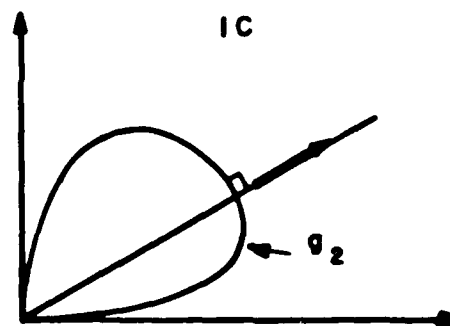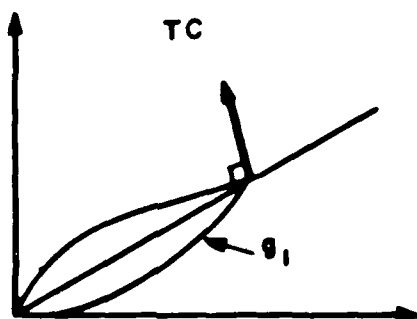
TC

g_1

IC

g_2

Fig.7. Schematic Plastic Potential Surfaces for Class 1 (TC) and Class 2 (IC) Loadings

29

loading stress increments (e.g. one-dimensional strain and isotropic compression) are concave toward the stress axis and exhibit stiffer behavior with increasing load. This is reflected in the different shapes of the hardening functions for Class 1 and Class 2 loadings as shown in Fig. 9.

Strength Model - An understanding of the strength of soils is essential to the formulation of general-purpose constitutive models for soils. Failure is a limiting case and should be defined first, so that the form of equations adopted for various elements of the constitutive model (the Class 1 hardening function in particular) will behave properly as limiting conditions are approached. The Mohr-Coulomb failure theory is used by most geotechical engineers to model the strength of soils. However, a more fundamental approach that considers the particulate nature of soils has been developed by Hardin (1985b) and will be used to represent cohesionless soil strength.

There are two fundamental mechanisms that govern the deformation of particulate materials: (1) bonding at particle contacts; and (2) the kinematics of particle movement within an element of deforming soil. In formulating constitutive equations for soils, the two parameters that represent the two basic particulate mechanisms are: (1) the bonding obliquity angle ϕ_o; and (2) the maximum rate of dilation d_{max}. Soil strength in terms of effective stress has been defined by Hardin (1985b) using these two parameters. The strength for cohesionless soils in triaxial compression is defined by

Triaxial Compression (TC)

$$d_{maxTC} = \frac{d_{o\sigma}}{1 + 7 \frac{\sigma'_3}{\sigma'_d}} - \frac{2d_n}{\frac{\sigma'_3}{\sigma'_d} + \frac{\sigma'_d}{\sigma'_3}} \qquad (4a)$$

$$\tan \phi_\mu = \tan \phi_{\mu o\sigma} \left[r_\sigma + \frac{(1 - r_\sigma)}{1 + \frac{\sigma'_3}{\sigma'_f}} \right] \qquad (4b)$$
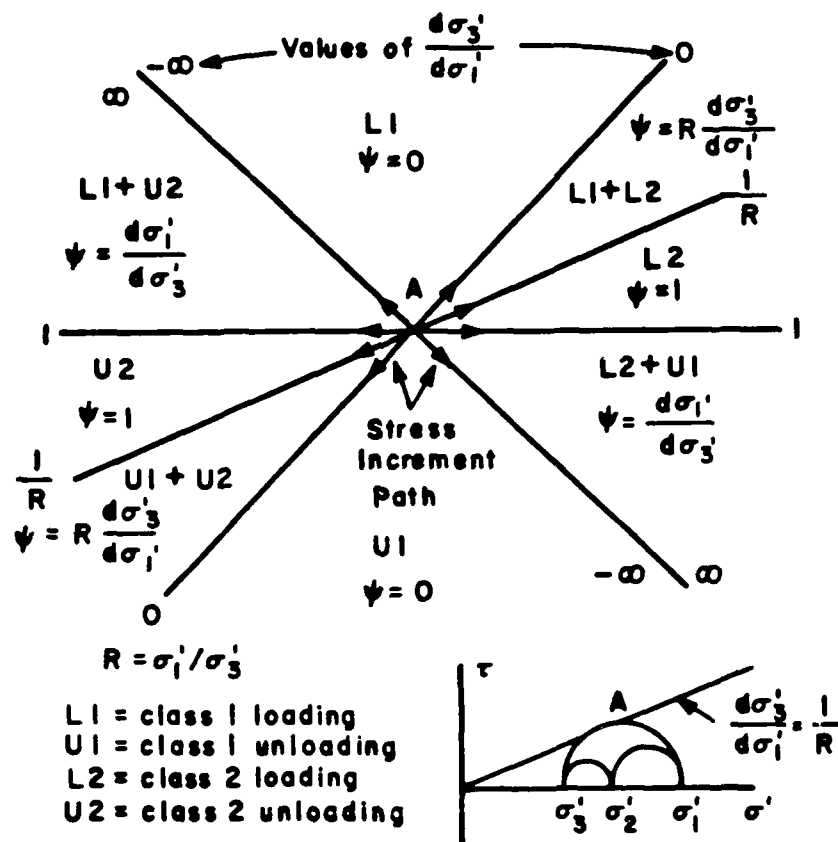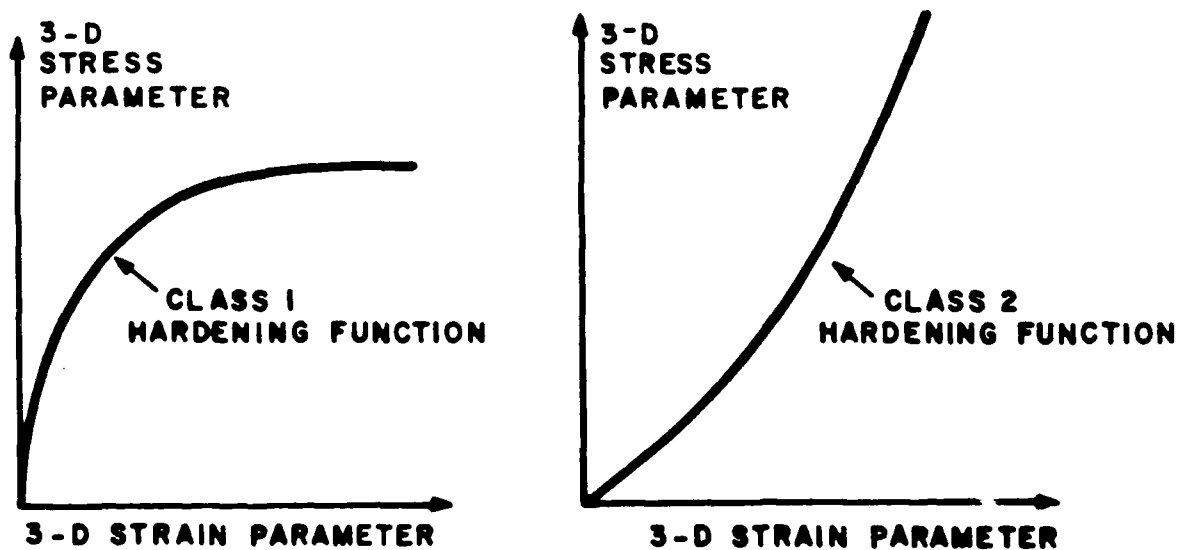
Fig. 8.   Definition of Loading

Fig. 9.   Class 1 and Class 2 Hardening Function Schematics

31

$$\sin \phi_{cv} = k_f \left(\frac{\pi}{2} - \phi_\mu \right) \tan \phi_\mu$$
$$+ \left(1 - k_f \right) \sin \phi_\mu \tag{4c}$$

$$K_{min} = \frac{1 + \sin \phi_\mu}{1 - \sin \phi_\mu} \tag{4d}$$

$$R_{cvTC} = \frac{1 + \sin \phi_{cv}}{1 - \sin \phi_{cv}} \tag{4e}$$

$$R_{maxTC} = R_{cvTC} + (2 K_{min} - R_{cvTC}) d_{maxTC} \tag{4f}$$

where d_{oo} is the value of d_{maxTC} at $\sigma_3' = 0$; d_n is a parameter related to the maximum negative rate of dilation; σ_d' is the dilation reference stress; σ_f' is the reference stress that defines the rate at which ϕ_μ decreases with increasing σ_3' ($\approx 10\ p_a$); ϕ_μ is the mineral friction angle which equals the bonding obliquity angle for cohesionless soil; $\phi_{\mu oo}$ is the value of ϕ_μ for $\sigma_3' = 0$; ϕ_{cv} is the critical state angle of shearing resistance; r_σ is a parameter which defines the effect of confinement on ϕ_μ; k_f is the critical state strength coefficient (≈ 0.60); K_{min} is the minimum energy transmission ratio; R_{cvTC} is the critical state principal stress ratio for triaxial compression loading; and R_{maxTC} is the maximum principal stress ratio for triaxial compression loading.

For an arbitrary computation stress path, the strength equations include (Hardin, 1985b):

Computation Path (CP)

$$b = \frac{1}{2} (1 - \sqrt{3} \tan \theta) \tag{5a}$$

$$m' = \frac{1}{1 + \log(R_{cvTC}(1 + d_{maxTC}))} \tag{5b}$$

$$F(b) = 4b^{m'}(1 - b^{m'}) \tag{5c}$$

$$R_{max} = R_{maxTC} + 2(R_{cvTC} - K_{min})\ F(b)\ d_{maxTC} \tag{5d}$$

where b is a parameter which defines the intermediate principal stress; m' is a power coefficient for the interpolation function $F(b)$; θ is the polar principal stress invariant (see Table 6); and R_{max} is the maximum

32

principal stress ratio. Equations 5 have generalized Eqs. 4 with respect to stress path through the interpolation function F(b). The interpolation function accounts for the effect of stress path on energy transmission and dissipation at the peak principal stress ratio. F(b) gives identical strengths in triaxial compression (b=0) and extension (b=1). It has also been chosen so that the value of b = $(\sigma'_2 - \sigma'_3)/(\sigma'_1 - \sigma'_3)$ for plane strain matches test results.

Class 1 Hardening and Softening - A Class 1 hardening/softening function defines the relationship between two scaler quantities representing 3D states of stress and plastic strain, respectively. The principal stress ratio R $(=\sigma'_1/\sigma'_3)$ has been used by Hardin and Blandford (1988b) to represent state of stress and Class 1 plastic work W^p_1 represents the state of plastic strain. Development of the hardening/softening function for general Class 1 loading requires that a relationship between R and W^p_1 that is independent of Class 1 stress paths be formulated.

Relationships between the normalized triaxial compression stress ratio $\tilde{r}_{TC}$ and the normalized triaxial compression plastic work $\tilde{W}^p_{TC}$ are

pre-peak behavior:

$$\tilde{W}^p_{TC} = 1 - (1 - \tilde{r}^\alpha_{TC})^\beta \tag{6a}$$

post-peak behavior:

$$\tilde{W}^p_{TC} = 1 + a_{TC} \left[\frac{1 - \tilde{r}_{TC}}{\tilde{r}_{TC} - \tilde{r}_{cvTC}} \right]^{m_{TC}} \tag{6b}$$

where

$$\tilde{r}_{TC} = \frac{R_{TC} - 1}{R_{maxTC} - 1} \tag{6c}$$

$$\tilde{r}_{cvTC} = \frac{R_{cvTC} - 1}{R_{maxTC} - 1} \tag{6d}$$

in which α, β, a_{TC} and m_{TC} are pre-peak and post-peak shape parameters. The normalized stress ratio and plastic work represent a relationship which is invariant for Class 1 stress paths (Hardin and Blandford,

1988b).

The normalized stress ratio, $\tilde{r}$, and normalized plastic work, $\tilde{W}_1^p$, for an arbitrary Class 1 stress path are defined as (Hardin and Blandford, 1988b)

$$\tilde{r} = \frac{R - 1}{\bar{R}_{max} - 1} \tag{7a}$$

$$\tilde{W}_1^p = f_1 \left[\frac{P_a}{\sigma_3'} \right]^{\lambda_1} \frac{W_1^p}{P_a} \tag{7b}$$

where

$$\bar{R}_{max} = R_{maxTC} + [R_{max} - R_{maxTC}] \, [1 - F(\tilde{r})]$$

$$F(\tilde{r}) = 4\tilde{r}^{\bar{n}} \, (1 - \tilde{r}^{\bar{n}})$$

$$\bar{n} = \frac{\log (0.5)}{\log \left[\dfrac{R_{cvTC} - 1}{R_{maxTC} - 1} \right]}$$

in which f_1 is a constant and λ_1 depends on d_{maxTC} and the initial void ratio e_o. Equation 7a is iteratively evaluated until $\tilde{r}$ converges and $\bar{R}_{max}$ is initially set equal to R_{max} calculated in the strength alogorithm (Eqs. 4 and 5).

Since the relationship between $\tilde{r}$ and $\tilde{W}_1^p$ is unique (i.e. independent of the Class 1 stress path), the following relationships hold (Hardin and Blandford, 1988b)

$$\tilde{r}_{TC} = \tilde{r} \tag{8a}$$

$$\tilde{W}_1^p = \tilde{W}_{TC}^p \tag{8b}$$

Equations 6-8 are used to express invariant plastic stiffness relationships in terms of triaxial compression relationships. Based on the triaxial compression developments, EPSAP simply calculates $\tilde{r}$ and $\tilde{W}_1^p = \tilde{W}_{TC}^p$ values to be used for calculating the Class 1 plastic work in Eq. 7b. The plastic work of Eq. 7b is used to calcuate the incremental plastic work which is used to calculate plastic strains for arbritrary

Class 1 stress paths as discussed following the next section.

Class 2 Hardening - The Class 2 hardening function also defines the relationship between two scaler quantities representing 3D states of stress and plastic strain, respectively. Normalized mean principal stress $\tilde{\sigma}'_m$ is used to represent the state of stress and the Class 2 normalized plastic work $\tilde{W}^p_2$ represents the state of plastic strain. A preliminary relationship between $\tilde{\sigma}'_m$ and $\tilde{W}^p_2$ that is independent of stress path for Class 2 loadings in terms of one-dimensional strain (see Tables 7, 8 and 9 for the one-dimensional strain model) is (Hardin and Blandford, 1988b are developing an analytic represenation which will be similar to the Class 1 stress path invariant relationship)

$$(\tilde{\sigma}'_m)_{1D} = (\tilde{\sigma}'_m)_{CP} \tag{9a}$$

$$(\tilde{W}^p_2)_{CP} = \tilde{W}^p_{1D} \tag{9b}$$

Normalized Class 2 plastic work $\tilde{W}^p_2$ is defined as follows

$$\tilde{W}^p_2 = \frac{(R_{max} - R)}{(R_{max} - 1)} \left[\frac{W^p_2}{p_a} \right]^{\lambda_2} \tag{10}$$

where λ_2 is a constant and $\tilde{\sigma}'_m \equiv \sigma'_m/p_a$. Based on the developed one-dimensional strain relationships, EPSAP simply reads in a table of $\tilde{\sigma}'_m$ and $\tilde{W}^p_{1D}$ values which are calculated based on the algorithms given in Tables 7 - 9. Cubic spline interpolation based on the $(\tilde{\sigma}'_m)_{CP}$ is used to calculate the normalize class 2 plastic work. The class 2 plastic work, W^p_2, is calculated from Eq. 10 which is used to calculate the increment in plastic work. Calculation of the Class 1 and Class 2 plastic strain increments depends on the incremental Class 1 and Class 2 plastic work and the gradients of the plastic potential surface. Details of these calculations are provided in the following section for arbitrary stress paths.

Class 1 and Class 2 Plastic Strain Computations - Equation 2 shows that

35

Table 7. Algorithm for 1D-Strain Total Work Potential
(notation is defined in Table 9)

Given: e_o, p, S_{1Dmax}, S_{1Dmin}, σ_b', σ_{CR}', m_{1D}, P_a, and $(\sigma_1')_{1D}$

Compute: ω_{1D} = 1D-strain total work potential at $(\sigma_1')_{1D}$

Step

1. $\sigma^* = \sigma_b'/e_o^2$

2. $S_{1D} = S_{1Dmax}$ for $(\sigma_1')_{1D} \leq \sigma^*$

$$S_{1D} = S_{1Dmin} + \frac{S_{1Dmax} - S_{1Dmin}}{1 + \left[\dfrac{e_o^2\,(\sigma_1')_{1D} - \sigma_b'}{\sigma_{CR}'}\right]^{m_{1D}}} \quad \text{for} \quad (\sigma_1')_{1D} > \sigma^*$$

3. $$e_{1D} = \frac{1}{\dfrac{1}{e_o} + \dfrac{1}{S_{1D}}\left[\dfrac{(\sigma_1')_{1D}}{P_a}\right]^p}$$

4. $\dfrac{dS_{1D}}{d(\sigma_1')_{1D}} = 0$ for $(\sigma_1')_{1D} \leq \sigma^*$

$$\frac{dS_{1D}}{d(\sigma_1')_{1D}} = \frac{-m_{1D}\,e_o^2(S_{1Dmax} - S_{1Dmin})}{\sigma_{CR}'} \frac{\left[\dfrac{e_o^2\,(\sigma_1')_{1D} - \sigma_b'}{\sigma_{CR}'}\right]^{m_{1D}-1}}{\left\{1 + \left[\dfrac{e_o^2\,(\sigma_1')_{1D} - \sigma_b'}{\sigma_{CR}'}\right]^{m_{1D}}\right\}^2}$$

for $(\sigma_1')_{1D} > \sigma^*$

5. $$\omega_{1D} = \frac{e_{1D}^2}{1 + e_{1D}}\left[\frac{(\sigma_1')_{1D}}{P_a}\right]^p \left[\frac{p}{S_{1D}} - \frac{(\sigma_1')_{1D}}{S_{1D}^2}\frac{dS_{1D}}{d(\sigma_1')_{1D}}\right]$$

Note: The constrained modulus $M = \dfrac{(\sigma_1')_{1D}}{\omega_{1D}}$

Table 8. Algorithm for 1D-Strain Elastic Work Potential and Plastic Principal Strain Increment Ratios (notation is defined in Table 9)

Given: ν, n, S_1, S_2, S_3, K_o, P_a, $(\sigma_1')_{1D}$, and e_{1D} and ω_{1D} (Table 7) where the 1D-strain test principal stress axes coincide with reference fabric principal axes for the soil, $[S_\sigma] = [\Sigma]$, $S_x = S_1$, $S_y = S_2$, $S_z = S_3$; and $K_o \leq 1$

Compute: ω_{1D}^e = 1D-strain elastic work potential at $(\sigma_1')_{1D}$; and

$$(d\epsilon_i^P/d\epsilon_1^P)_{1D}, \quad i = 2, 3, \quad \text{1D-strain plastic principal strain increment ratios}$$

Step

1. $c_1^* = \dfrac{1}{S_1} - \nu\, K_o^{1-n}\left[\dfrac{1}{S_2} + \dfrac{1}{S_3}\right]$

2. $c_2^* = \dfrac{K_o^{1-n}}{S_2} - \nu\left[\dfrac{1}{S_1} + \dfrac{K_o^{1-n}}{S_3}\right]$

3. $c_3^* = \dfrac{K_o^{1-n}}{S_3} - \nu\left[\dfrac{1}{S_1} + \dfrac{K_o^{1-n}}{S_2}\right]$

4. $c^* = c_1^* + K_o\,(c_2^* + c_3^*)$

5. $k_{1D}^* = (0.3 + 0.7\, e_{1D}^2)\left[\dfrac{(\sigma_1')_{1D}}{P_a}\right]^{1-n}$

6. $\omega_{1D}^e = c^*\, k_{1D}^*$

7. $\left[\dfrac{d\epsilon_i^e}{d\epsilon_1}\right]_{1D} = \dfrac{c_1^*\, k_{1D}^*}{\omega_{1D}}, \qquad i = 1, 2, 3$

8. $\left[\dfrac{d\epsilon_i^P}{d\epsilon_1^P}\right]_{1D} = \dfrac{-\left[\dfrac{d\epsilon_i^e}{d\epsilon_1}\right]_{1D}}{1 - \left[\dfrac{d\epsilon_1^e}{d\epsilon_1}\right]_{1D}}, \qquad i = 2, 3$

37

Table 9. Algorithm for 1D-Strain Normalized Stress and Plastic Work

---

Given: $(\sigma'_1)_{1D}$, K_o, λ_2, ω_{1D} and ω^e_{1D} as functions of σ'_1 from Tables 7 and 8; and p_a

Compute: $\tilde{\sigma}'_{1D}$ = normalized stress; and $\tilde{W}^p_{1D}$ = normalized plastic work

Step

1. $\tilde{\sigma}_{1D} \equiv (\tilde{\sigma}'_m)_{1D} = \dfrac{(\sigma'_1)_{1D}}{3\,p_a}\,(1 + 2\,K_o)$

2. Compute R_{maxTC} for $\sigma'_3 = K_o(\sigma'_1)_{1D}$ using the Eq. 4f

3. $W^p_{1D} = \displaystyle\int_0^{(\sigma'_1)_{1D}} (\omega_{1D} - \omega^e_{1D})\,d\sigma'_1$

4. $\tilde{W}^p_{1D} = \dfrac{\left[R_{maxTC} - \dfrac{1}{K_o}\right]}{(R_{maxTC} - 1)}\left[\dfrac{W^p_{1D}}{p_a}\right]^{\lambda_2}$

Notation for Tables 7 - 9

$(\sigma'_1)_{1D}$ = major principal stress for 1D-strain loading;

ν = elastic Poisson ratio;

S_i = principal direction elastic stiffness coefficients (i=1,2,3);

n = stress power coefficient;

p = void ratio/total work potential power coefficient;

S_{1Dmax} = maximum dimensionless stiffness coefficient for 1D-strain;

S_{1Dmin} = minimum dimensionless stiffness coefficient for 1D-strain;

σ'_b = crushing mechanism break point stress;

σ'_{CR} = crushing mechanism reference stress;

m_{1D} = power coefficient used to calculate the dimensionless 1D-strain stiffness;

S_{1D} = dimensionless 1D-strain stiffness;

e_o = zero principal stress void ratio;

e_{1D} = 1D-strain void ratio;

K_o = lateral effective stress coefficient for 1D-strain; and

λ_2 = Class 2 plastic work power coefficient.

the Class 1 and Class 2 plastic strain increments can be evaluated in terms of the derivatives of the plastic potential functions with respect to the effective stresses. However, it is not necessary to explicitly define the plastic potential functions in terms of the effective stresses and then differentiate. Rather, you can work directly in terms of the gradients of the plastic potential functions and express the plastic strain increments as (Hardin and Blandford, 1988b)

$$\{d\epsilon^P\}_k = d\lambda_k^h \ \{g'\}_k \tag{11}$$

where

$$\{g'\}_k = \lfloor \ g_x' \quad g_y' \quad g_z' \quad g_{xy}' \quad g_{yz}' \quad g_{zx}' \ \rfloor_k^T$$

in which $\{g'\}_k$ is the vector of plastic potential function gradients represented in Eq. 2.

The plastic potential function gradients are a function of the principal plastic strain ratios (Hardin and Blandford, 1988b). Consequently, the first step in computing the gradient functions is to calculate the normalized principal plastic strain ratios. Class 1 normalized principal plastic strain ratios $((\bar{g}_i')_1 \equiv (d\epsilon_i^P/d\epsilon_1^P)_1; \ i = 1,2,3)$ are evaluated as

$$(\bar{g}_1')_1 = 1 \tag{12a}$$

$$(\bar{g}_2')_1 = -\frac{D}{2} + (1 + \frac{D}{2}) \ b^{\zeta_2} \tag{12b}$$

$$(\bar{g}_3')_1 = -\frac{1}{2} (1 + 3b^{\zeta_3}) \frac{D}{2} \tag{12c}$$

where

$$\zeta_2 = \frac{\log \left[\frac{D}{D+2} \right]}{\log (b_{ps}^p)}$$

$$\zeta_3 = \frac{\log (1/3)}{\log (b_{ps}^p)}$$

39

$$b_{ps}^p = \tilde{r} \, (0.5)^{\frac{1}{\tilde{m}'}} + 0.5 \, (1 - \tilde{r})$$

The parater D represents the stress-dilatancy behavior of cohesionless soils and is expressed as (Hardin and Blandford, 1988b)

prepeak:
$$D = (1 + d_{maxTC}) \frac{R}{R_{max}} - C_{v1} \frac{R}{R_{max}} \left[1 - \frac{R}{R_{max}} \right] \qquad (13a)$$

postpeak:
$$D = 1 + d_{maxTC} \left[\frac{R - R_{cvTC}}{R_{max} - R_{cvTC}} \right] \qquad (13b)$$

Note that the maximum rate of dilation occurs at the peak. Parameter C_{v1} is used to define a parabolic pre-peak stress-dilatancy relationship and b_{ps}^p is the value of b for plane plastic strain.

The Class 2 normalized principal plastic strain ratios are (Hardin and Blandford, 1988b)

$$(\bar{g}_1')_2 = 1 \qquad (14a)$$

$$(\bar{g}_i')_2 = (\bar{g}_i')_1 + \left[1 - \left[\frac{d\epsilon_i^p}{d\epsilon_1^p} \right]_{1D} \right] \left[\frac{1}{R} \right]^{\eta_i} \quad ; \quad i = 2,3 \qquad (14b)$$

where

$$\eta_i = \frac{\log \left[\frac{2 \left[\frac{d\epsilon_i^p}{d\epsilon_1^p} \right]_{1D} + D}{2 + D} \right]}{\log (K_o)} \quad ; \quad i = 2,3$$

K_o is the lateral effective stress coefficient for one-dimensional strain (1D); and $(d\epsilon_i^p/d\epsilon_1^p)_{1D}$ are the one-dimensional strain principal plastic strain increment ratios as given in Table 8 for $i = 2, 3$.

The plastic potential function gradients of Eq. 11 are calculated in terms of the principal normalized strain ratios as

$$\{g'\}_k = [R_\epsilon]^{-1} \{\bar{g}'\}_k \qquad (15)$$

40

where

$$\{\bar{g}'\}_k = \lfloor \bar{g}'_1 \quad \bar{g}'_2 \quad \bar{g}'_3 \quad 0 \quad 0 \quad 0 \rfloor_k^T$$

and $[R_\epsilon]^{-1}$ is given in Table 5.

With the plastic strain ratios computed from Eq. 15, the plastic strain increments are calculated from Eq. 11 where

$$d\lambda_k^h = \frac{dW_k^p}{S_{rk}} \tag{16a}$$

$$S_{rk} = \lfloor \hat{\sigma}' \rfloor \{g'\}_k \tag{16b}$$

$$\lfloor \hat{\sigma}' \rfloor = \lfloor \sigma'_x \quad \sigma'_y \quad \sigma'_z \quad \tau_{xy} \quad \tau_{yz} \quad \tau_{zx} \rfloor^T \tag{16c}$$

and ^ signfies that the quantity is evaluated as the midpoint of the increment. The plastic strain increments computed from Eq. 11 are used in Eq. 3 to calculate the total plastic strain increment.

FINITE ELEMENT FORMULATION

Finite element stiffness analyses are based on generating element force-displacement equations and then assembling the element equations to represent the soil medium equilibrium equations. Equilibrium equations for nonlinear problems are typically stated in incremental form. Generation of the incremental finite element stiffness equations requires proper representation of the total incremental strain vector $\{\Delta\epsilon\}$ and the incremental effective stress vector $\{\Delta\sigma'\}$ where Δ symbolizes finite increment. The total incremental strains are expressed as the sum of the incremental elastic strain vector $\{\Delta\epsilon^e\}$ and the incremental plastic strain vector $\{\Delta\epsilon^p\}$, i.e.

$$\{\Delta\epsilon\} = \{\Delta\epsilon^e\} + \{\Delta\epsilon^p\} \tag{17}$$

Substituting Eq. 1 into Eq. 17 and solving for the incremental effective stress vector leads to

$$\{\Delta\sigma'\} = [S]^{-1} (\{\Delta\epsilon\} - \{\Delta\epsilon^p\})$$

41

$$= [C_E] \{\Delta\epsilon\} - [C_E] \{\Delta\epsilon^P\} \qquad (18)$$

where $[C_E] = [S]^{-1} = p_a^{1-n}/F(e) \ ([R_\sigma]^{-1} [\Sigma]^{-1} [R_\sigma] [S_f]^{-1} [S_\nu]^{-1})$ is the nonlinear elastic material stiffness matrix and the inverse matrices can be deduced from Tables 3 - 5; and $\{\Delta\epsilon^P\}$ is obtained from Eq. 3.

Assuming that the initial state of the soil medium is at stress level $\{\sigma_0'\}$, the incremental equilibrium condition at the end of load step $m+1$ is expressed in terms of the virtual work principle for small strains as (Washizu, 1968)

$$\int_\Omega {}^{m+1}\lfloor\sigma'\rfloor \ \delta(\{\Delta\epsilon\}) \ d\Omega - \int_{\Gamma_t} {}^{m+1}\lfloor t\rfloor \ \delta(\{\Delta u\}) \ d\Gamma = 0 \qquad (19)$$

where δ symbolizes virtual operator; $\{\Delta\epsilon\}$ is the change in the total strain between load step m and $m+1$ due to the increment in the tractions $\{\Delta t\}$ $(\{t\} = \lfloor t_x \ t_y \ t_z \rfloor^T)$; $\{u\}$ is the three-dimensional displacement vector $(= \lfloor u_x \ u_y \ u_z \rfloor^T)$; Ω is the domain (volume); Γ_t is the traction loaded boundary (surface and line); and the pre-superscript indicates the load step with m being the previous load step and $m+1$ being the current load step. Body force terms have been neglected in Eq. 19 since they are assumed to be included in the initial stress vector. The incremental virtual work expression is obtained from Eq. 19 by substituting

$$
\begin{aligned}
{}^{m+1}\{\sigma'\} &= {}^{m}\{\sigma'\} + \{\Delta\sigma'\} \\
{}^{m+1}\{t\} &= {}^{m}\{t\} + \{\Delta t\}
\end{aligned}
\qquad (20)
$$

which leads to

$$\int_\Omega \lfloor\Delta\sigma'\rfloor \ \delta(\{\Delta\epsilon\}) \ d\Omega - \int_{\Gamma_t} \lfloor\Delta t\rfloor \ \delta(\{\Delta u\}) \ d\Gamma = 0 \qquad (21)$$

Utilizing the usual isoparametric approach to finite element analysis (see Appendix I), the incremental displacements and strains are related to the element displacements as

$$\{\Delta u\} = [N] \ \{\Delta p\}$$

$$\{\Delta\epsilon\} = [B] \{\Delta p\} \qquad\qquad \dots \quad (22)$$

where $[N]$ is the matrix of shape functions describing the element displacement variations; $\{\Delta p\}$ is the element incremental displacement vector; and $[B]$ is the element strain-displacement matrix assuming small strains and positive compressive strains. Details for the $[N]$ and $[B]$ matrices are given in Appendix I. Substituting Eqs. 18 and 22 and into Eq. 21 results in

$$[k_E] \{\Delta p\} = {}^{m+1}(\Delta\ell) \{f\} + \{\Delta f^P\} \qquad (23)$$

where

$$[k_E] = \int_{\Omega_e} [B]^T [C_E] [B] \, d\Omega$$

(element elastic stiffness matrix)

$$\{f\} = \int_{\Gamma_{el}} [N_1]^T \{t_1\} \, d\Gamma_1 + \int_{\Gamma_{es}} [N_s]^T \{t_s\} \, d\Gamma_s$$

(element elastic load vector)

$$\{\Delta f^P\} = \int_{\Omega_e} [B]^T [C_E] \{\Delta\epsilon^P\} \, d\Omega$$

(element incremental plastic load vector)

Additionally, ${}^{m+1}(\Delta\ell)$ is the incremental load step multiplier; subscripts e, 1 and s signify element, line and surface, respectively; matrices $[N_1]$ and $[N_s]$ are given in Appendix I; and the other symbols retain their previously defined interpretations. Due to the isoparametric implementation of the elements shown in Fig. 5, the element integrals in Eq. 23 are evaluated numerically using standard two point Gauss-Legendre quadrature in each coordinate direction (see Appendix I).

Accumulating Eq. 23 for all the elements leads to

$$[K_E] \{\Delta p\} = {}^{m+1}(\Delta\ell) \{P\} + \{\Delta P^P\} \qquad (24)$$

The matrices of Eq. 24 are defined as

43

$$[K_E] = \Sigma \ [k_E]$$

(system elastic stiffness matrix)

$$\{P\} = \{P_C\} + \Sigma \ \{f\}$$

(system elastic load vector)

$$\{\Delta P^P\} = \Sigma \ \{\Delta f^P\}$$

(system incremental plastic load vector)

in which Σ signifies summation over the elements consistent with direct stiffness assembly; and $\{P_C\}$ is the applied concentrated force vector. Condensation of the internal degrees of freedom is applied to the modified hexahedron element prior to assembly in Eq. 24 (see Appendix I for details). Unlike most finite element stiffness equations, the discretized equations of Eq. 24 are nonsymmetric. This nonsymmetry in the stiffness equations is due to the nonsymmetric constitutive relations of the elastic constitutive matrix, $[C_E]$.

The direct solution of Eq. 24 (solution is used generically here, the nonlinear solution strategy is presented in the next section) would be enormous due to the *large number of simultaneous equations*. Consequently, the direct stiffness assembly and solution procedure is based on the unsymmetric profile (or skyline) algorithm of Taylor (1977). Taylor's solution algorithm incorporates the symmetry of the coefficient locations with respect to the diagonal plus the variable band structure of the nonsymmetric finite element equations. Taylor's algorith has been written for memory resident storage and solution. Thus, to accomodate the large number of equations which are encountered in solving typical three-dimensional problems, Taylor's algorithm has been modified for out-of-core (or virtual memory) assembly and solution.

NONLINEAR SOLUTION ALGORITHM

The incremental/iterative solution procedure used to solve the finite element discretized equations of Eq. 24 for three-dimensional elasto-plastic cohesionless soil problems is discussed in this section. Solution of the nonlinear equations is based on a stepwise linearization of the equations via an incremental/iterative predictor-midpoint corrector scheme which includes geometric updates at each iteration. Updating

the geometry provides a natural (true) stress/strain representation in the context of the small strain formulation presented in the previous section (Hsu, 1986). The natural stress/strain formulation is required to be consistent with the elasto-plastic constitutive equations developed in Hardin and Blandford (1988a,b). This solution scheme can be classified as an initial stress approach (e.g. Zienkiewicz, 1977) for solving elasto-plastic problems due to the elastic formulation of Eq. 24. However, rather than solve for iterative changes in the displacements, strains and stresses (as is usual with the initial stress approach) the solution for the full incremental values will be generated based on the midpoint stiffness properties. Utilization of midpoint constitutive properties is equivalent to using a second-order iterative corrector scheme (Zienkiewicz, 1977).

The general solution strategy in the load-displacement space can be written as

$$\overline{m}[K_E]^{(i-1)} \{\Delta p\}^{(i)} = {}^{m+1}(\Delta \ell) \, \overline{m}\{P\}^{(i-1)} + \overline{m}\{\Delta P^P\}^{(i-1)} \qquad (25)$$

where $\overline{m}$ signifies the midpoint load level (i.e. $\overline{m}$ is midway between the previous load step m and the current load step $m+1$); and the parenthetical superscript signifies the iteration number. Evaluation of the element stiffness matrices and load vectors used in Eq. 25 are obtained by substituting

$$\Omega_e \equiv \overline{m}\Omega_e^{(i-1)} \quad , \quad [B] \equiv \overline{m}[B]^{(i-1)}$$

$$ \qquad (26)$$

$$\Gamma_{el} \equiv \overline{m}\Gamma_{el}^{(i-1)} \quad , \quad \Gamma_{es} \equiv \overline{m}\Gamma_{es}^{(i-1)}$$

into Eq. 24. The midpoint geometry for iteration i is calculated by updating the nodal coordinate vector $\{x\}$ ($\{x\} = \lfloor x_n \; y_n \; z_n \rfloor^T$ where subscript n represents node point n) as

$$\overline{m}\{x\}^{(i)} = {}^{m}\{x\} + \frac{1}{2} \{\Delta p\}^{(i)} \qquad (27)$$

Equations 25-27 are expressed in terms of the midpoint corrector

iteration strategy. The predictor step is obtained for $i = 1$ and $\bar{m} = m$ which results in

$$\bar{m}[K_E]^{(0)} = {}^m[K_E] \quad , \quad \bar{m}\{\Delta P^p\}^{(0)} = \{0\}$$

$$\bar{m}\Omega_e^{(0)} = {}^m\Omega_e \quad , \quad \bar{m}[B]^{(0)} = {}^m[B] \tag{28}$$

$$\bar{m}T_{el}^{(0)} = {}^mT_{el} \quad , \quad \bar{m}T_{es}^{(0)} = {}^mT_{es}$$

$$\bar{m}\{x\}^{(0)} = {}^m\{x\}$$

Equation 28 shows that the predictor step is based on the converged results obtained for load step m.

The displacement vector solution of Eq. 25 is written as the sum of the incremental elastic displacement vector $\{\Delta p^e\}$ and the incremental plastic displacement vector $\{\Delta p^p\}$, i.e.

$$\{\Delta p\}^{(i)} = \{\Delta p^e\}^{(i)} + \{\Delta p^p\}^{(i)} \tag{29}$$

where

$$\{\Delta p^e\}^{(i)} = {}^{m+1}(\Delta \ell) \left[\bar{m}[K_E]^{(i-1)} \right]^{-1} \bar{m}\{P\}^{(i-1)}$$

$$\{\Delta p^p\}^{(i)} = \left[\bar{m}[K_E]^{(i-1)} \right]^{-1} \bar{m}\{\Delta P^p\}^{(i-1)}$$

In order to evaluate Eq. 29, ${}^{m+1}(\Delta \ell)$ must be known. Startup (i.e. the first load increment) of the predictor-midpoint corrector algorithm is based on specifying ${}^1(\Delta \ell)$, i.e. the initial incremental load step. The load increment is adjusted in subsequent load steps by borrowing a scheme recommended by Ramm (1981) for arc-length algorithms, i.e.

$$^{m+1}(\Delta \ell) = {}^m(\Delta \ell) \sqrt{\frac{I_d}{{}^mI}} \tag{30}$$

where ${}^m(\Delta \ell)$ is the mth load step increment, ${}^mI$ is the number of iterations required to achieve equilibrium for the mth load step and I_d is

46

the desired number of iterations ($I_d \approx 3 - 5$). This strategy automatically leads to smaller load steps in areas of severe nonlinearity and longer lengths when the response is nearly linear. An upper limit of $^1(\Delta \ell)$ is imposed on Eq. 30 to reduce potential solution drift from the equilibrium curve.

Accumulated variable quantities through iteration i for load step m+1 are defined as

$$^{m+1}\{p\}^{(i)} = {}^m\{p\} + \{\Delta p\}^{(i)}$$

$$^{m+1}\{p^e\}^{(i)} = {}^m\{p^e\} + \{\Delta p^e\}^{(i)}$$

$$^{m+1}\{p^p\}^{(i)} = {}^m\{p^p\} + \{\Delta p^p\}^{(i)}$$

$$^{m+1}\{\sigma'\}^{(i)} = {}^m\{\sigma'\} + \{\Delta \sigma'\}^{(i)}$$

$$^{m+1}\{\epsilon\}^{(i)} = {}^m\{\epsilon\} + \{\Delta \epsilon\}^{(i)} \tag{31}$$

$$^{m+1}\{\epsilon^e\}^{(i)} = {}^m\{\epsilon^e\} + \{\Delta \epsilon^e\}^{(i)}$$

$$^{m+1}\{\epsilon^p\}^{(i)} = {}^m\{\epsilon^p\} + \{\Delta \epsilon^p\}^{(i)}$$

$$^{m+1}\{x\}^{(i)} = {}^m\{x\} + \{\Delta p\}^{(i)}$$

The incremental elastic strains and effective stresses are calculated as

$$\{\Delta \epsilon^e\}^{(i)} = {}^{\overline{m}}[B]^{(i)} \{\Delta p^e\}^{(i)}$$

$$\{\Delta \sigma'\}^{(i)} = [C_E({}^{\overline{m}}\sigma^{(i-1)})] \{\Delta \epsilon^e\}^{(i)} \tag{32}$$

Calculation of incremental rather than iterative strains and stresses in Eq. 32 is recommended by Key et al. (1981) for materials which involve path dependency. Midpoint effective stresses used in the elastic material stiffness matrix are calculated as

$$^{\overline{m}}\{\sigma'\}^{(i)} = {}^m\{\sigma'\} + \frac{1}{2}\{\Delta \sigma'\}^{(i)} \tag{33}$$

Termination of the iterations in Eq. 25 is based on an internal energy criterion (Bathe and Cimento, 1980). The incremental internal

energy criterion is

$$\frac{\lfloor \delta p \rfloor^{(i)} \, \bar{m}_{\{P\}}^{(i-1)}}{\lfloor \Delta p \rfloor^{(1)} \, m_{\{P\}}} < \epsilon_E \tag{34}$$

where ϵ_E is the energy error tolerance $(1 \times 10^{-8} \leq \epsilon_E \leq 1 \times 10^{-4})$; and $\lfloor \delta p \rfloor^{(i)E} = \lfloor \Delta p \rfloor^{(i)} - \lfloor \Delta p \rfloor^{(i-1)}$ which is the iterative change in the displacement vector.

Evaluating the elasto-plastic constitutive equations requires an accurate determination of the element stresses. The element incremental strains and stresses of Eq. 32 are evaluated at the element centroidal quadrature point which is the optimum location for elements which only contain complete linear polynomial representations (Barlow, 1976). Furthermore, centroidal stress and strain computations with the modified hexahedron element eliminate the necessity of recovering the condensed bubble mode displacements since their contribution is zero at the element centroid (Hughes, 1987). Further details on stress evaluations is provided in Appendix I.

CONSTITUTIVE EQUATION COMPUTATIONAL DETAILS

Natural elastic strain modeling requires that the void ratio e be upadated to reflect changes in the soil volume. The initial void ratio, e_i ($\equiv e_o$), is defined as

$$e_i = \frac{V_{vi}}{V_s} \tag{35}$$

where V_{vi} is the initial volume of voids; V_s is the solid volume which is assumed to be constant; and $V_i = V_{vi} + V_s$ is the initial soil volume. Since the initial void ratio can be measured, the volume of solids is calculated as

$$V_s = \frac{V_i}{1 + e_i} \tag{36}$$

Calculation of the void ratio at load level $\bar{m}$, iteration i is obtained as

48

$$\bar{m}_e(i) = \frac{\bar{m}_V(i) - V_s}{V_s} \qquad (37)$$

where $\bar{m}_V(i)$ is the centroidal element volume for iteration i corresponding to load level $\bar{m}$. Calculation of the iterative void ratio at the element centroid is consistent with the calculation of the constitutive properties. The updated void ratio of Eq. 37 is used in elastic soil function F(e) as given in Eq. 1.

If an anlysis is experiencing pure Class 1 loading, EPSAP prevents the incremental load from experiencing sudden loading to softening behavior in the same step. That is, if $^{m+1}\tilde{r}(1)$ is calculated to be greater than one in the predictor step then the load multiplier $^{m+1}\Delta\ell$ is calculated as

$$^{m+1}\Delta\ell = {}^{m+1}\Delta\ell_p \left[1 - \frac{{}^{m+1}\tilde{r}(1) - 1}{{}^{m+1}\tilde{r}(1) - {}^m\tilde{r}} \right] \qquad (38)$$

to ensure that the calculated $^{m+1}\tilde{r}$ will equal one and $^{m+1}\Delta\ell_p$ is calculated from Eq. 30. The scaling represented in Eq. 38 has been implemented to distinguish between loading and softening Class 1 behavior. Class 1 behavior after the scaling of Eq. 38 is in the softening range.

In addition, EPSAP allows for the input of arbitrary stress path loading. This is accomplished by treating the applied load as a quasi-time-dependent function. The piecewise linear varying loads are input in terms of the total magnitudes for a given load interval. For each load sequence, different increasing load magnitudes can be specified as well as different initial load step multipliers. This allows the analysis to build up the initial state of stress from an initial zero state of stress, for example.

VERIFICATION OF NUMERICAL PROCEDURES

A sequence of analyses is presented to verify EPSAP. The problems considered are shown in Fig. 10. Figure 10(a) represents constant b

stress paths to locate plane strain stress states. Figure 10(b) represents constant K stress paths which is used to locate one-dimensional strain. Both problem sets of Fig. 10 represent homogenous stress/strain problems. Hence, only a single hexahedron element discretization for $1/8^{th}$ of the symmetric problem is required. The material properties used for all analyses are:

$$p_a = 1.00 \qquad n = 0.50 \qquad \nu = 0.10$$
$$S_x = S_y = S_z = S_{xy} = S_{yz} = S_{zx} = 1400$$

$$d_n = 0.20 \qquad d_{o\sigma} = 1.0$$
$$\sigma'_d = 15 \qquad \sigma'_f = 10$$
$$\phi_\mu = 35° \qquad r_\sigma = 0.70 \qquad k_f = 0.60$$

$$\alpha = 2.00 \qquad \beta = 0.24$$
$$a_{TC} = 1.00 \qquad m_{TC} = 0.50 \qquad \lambda_1 = 1.50$$

$$e_o = 0.50 \qquad K_o = 0.50$$
$$\sigma'_b = 8 \qquad \sigma'_{CR} = 15$$
$$S_{1Dmax} = 40 \qquad S_{1Dmin} = 10$$
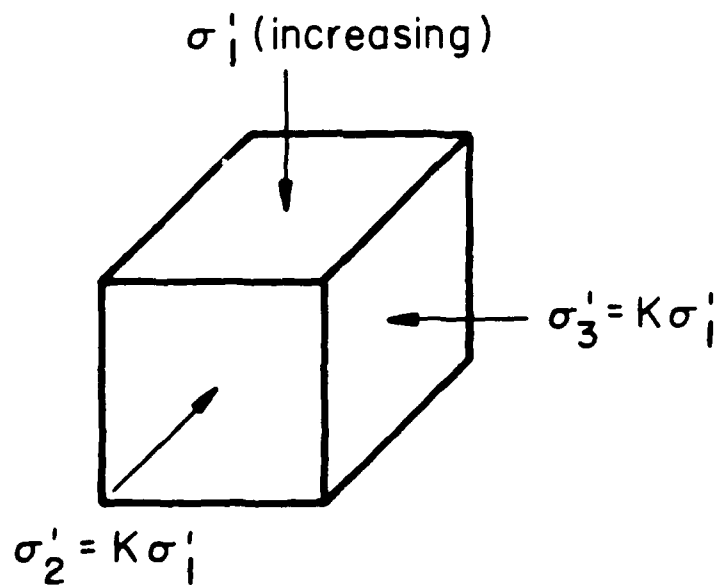$$m_{1D} = 1.50 \qquad p = 0.50 \qquad \lambda_2 = 0.71$$

which represent typical soil material properties but do not correspond to any particular test results for a soil specimen. A convergence tolerance of $\epsilon_E = 1 \times 10^{-8}$ is used for all analyses.

Considering the constant b stress paths (Fig. 10a), the principal stresses are increment isotropically to $\sigma'_1 = \sigma'_2 = \sigma'_3 = 1\ p_a$, followed by constant b loading where σ'_3 is constant, σ'_1 is increasing and $\sigma'_2 = b\sigma'_1 + (1-b)\sigma'_3$. Development of the initial state of stress is based on a reference state of stress of zero, i.e. $\{\sigma_o\} = \{0\}$, and isotropic compression stress increments of 0.001 p_a ($\Delta\ell = 0.001$) for ten load steps followed by isotropic compression stress increments of 0.01 p_a ($\Delta\ell = 0.01$) until $\sigma'_1 = \sigma'_2 = \sigma'_3 = 1\ p_a$. This is followed by constant b stress paths with stress increments of 0.01 p_a ($^1\Delta\ell = 0.01$). Results for the constant b stress path analyses are shown in Fig. 11-13 for b = 0 (triaxial compression), b = 1/2 (intermediate) and b = 1 (triaxial

σ_1' (increasing)
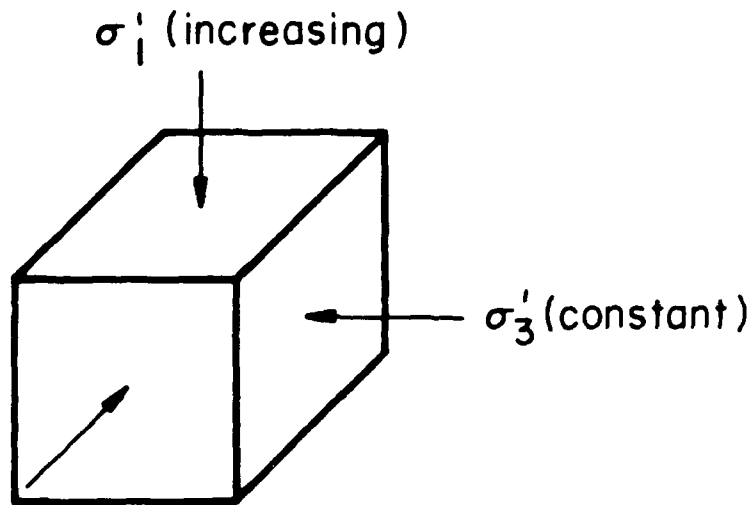
σ_3' (constant)

$$\sigma_2' = b\sigma_1' + (1-b)\sigma_3'$$

(a) Constant b Stress Paths ($0 \leq b \leq 1$)

σ_1' (increasing)

$\sigma_3' = K\sigma_1'$

$\sigma_2' = K\sigma_1'$

(b) Constant K Stress Path ($1/4 \leq K < 1$)

Fig. 10.   Load Path Definitions

extension). Figure 11 shows the plot of the major principal stress (σ_1') versus the major principal elastic strain, ϵ_1^e, for the three values of b. Figure 11 shows that increasing elastic stiffness in the direction of major principal stress increases with σ_1'. Furthermore, Fig. 11 shows the difference in elastic loading and unloading curves that results from the changing void ratio. Figure 12 presents the major principal stress versus the major principal strain, ϵ_1, for the same three values of b. Figure 12 shows that the model is capable of representing the increased strength associated with intermediate b stress paths (1 > b > 0), shifting of the peak strain and the work softening behavior. Figure 13 shows a plot of the negative plastic volumetric strain ($-\epsilon_{vol}^p$) versus the major principal plastic strain (ϵ_1^p). As should be expected, the triaxial extension analysis exhibits the greatest volumetric change with increasing major principal plastic strain. Figure 13 shows that the soil initially experiences volume compression which is then followed by volume expansion.

Considering next the constant K stress paths (Fig. 10b), the major principal stress increments are specified to be 0.001 p_a until σ_1' = 0.01 p_a, 0.01 p_a until σ_1' = 0.10 p_a and 0.10 p_a until σ_1' = 25 p_a. Principal stresses σ_2' = σ_3' = K σ_1'. Results for the one-dimensional strain (K = 1/2) and isotropic compression (K = 1) stress paths are shown in Figs. 14-16. Figures 14, 15 and 16 show plots of the major principal stress versus the major principal elastic strain; major principal stress versus the major principal strain; and the negative plastic volumetric strain versus the major principal plastic strain, respectively. These figures show that the computed elastic strains are nearly equal (Fig. 14) whereas the plastic strains are much smaller for the isotropic compression analysis compared with the one-dimensional strain analysis (Figs. 15 and 16). The decreased plastic behavior associated with isotropic compression should be anticipated due increased confinement. Figures 14 and 15 clearly show the concavity of Class 2 stress-strain curves towards the stress axis and exhibit increased stiffness with increasing load. Figure 16 shows that for isotropic or one-dimensional strain loadings, the soil exhibits nearly linear volume compression.

Fig. 11. Elastic Stress-Strain Results for Three
Class 1 Loadings

Fig. 12.   Total Stress-Strain Results for Three
Class 1 Loadings

Fig. 13. Negative Volumetric Plastic Strain –
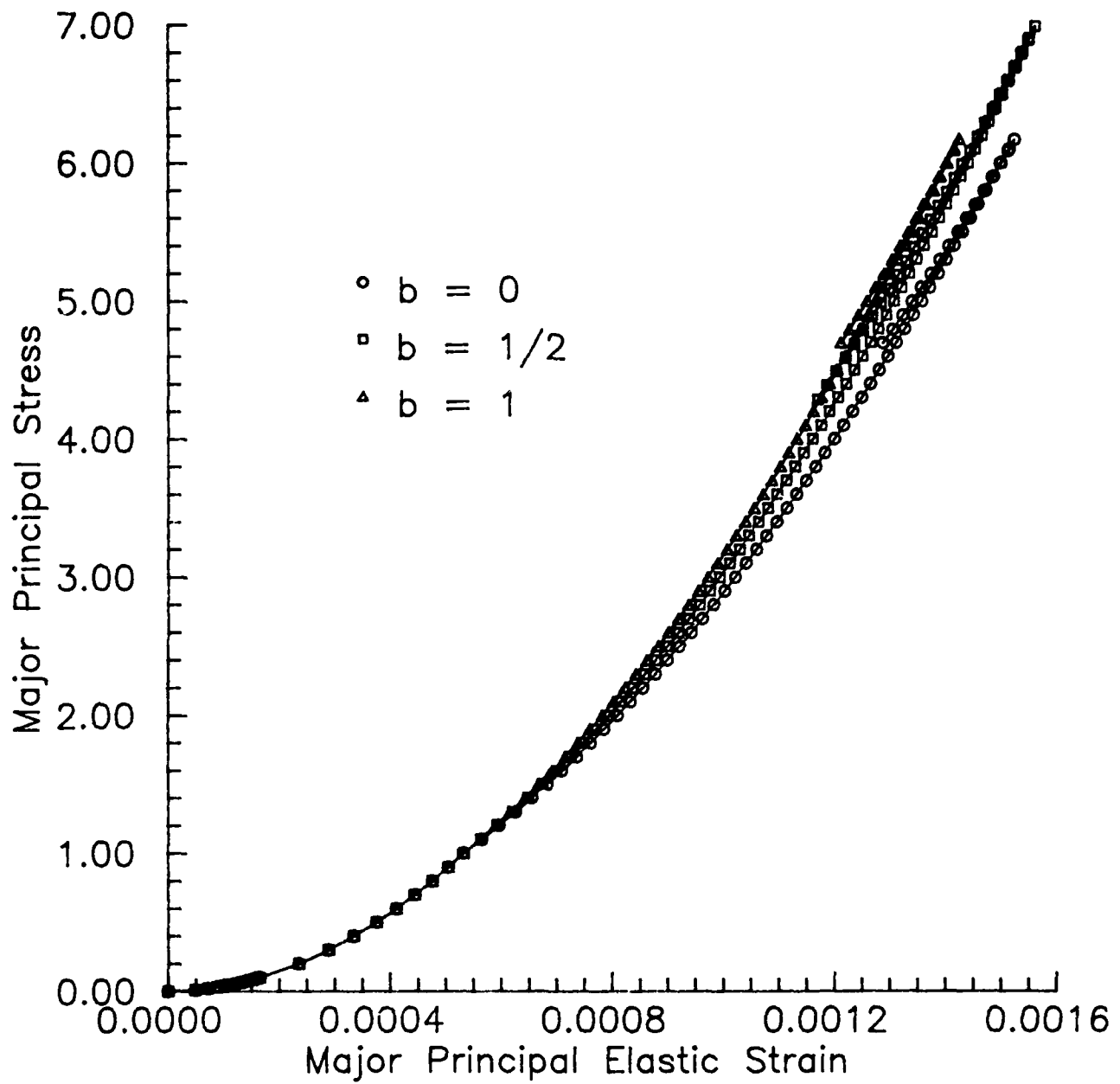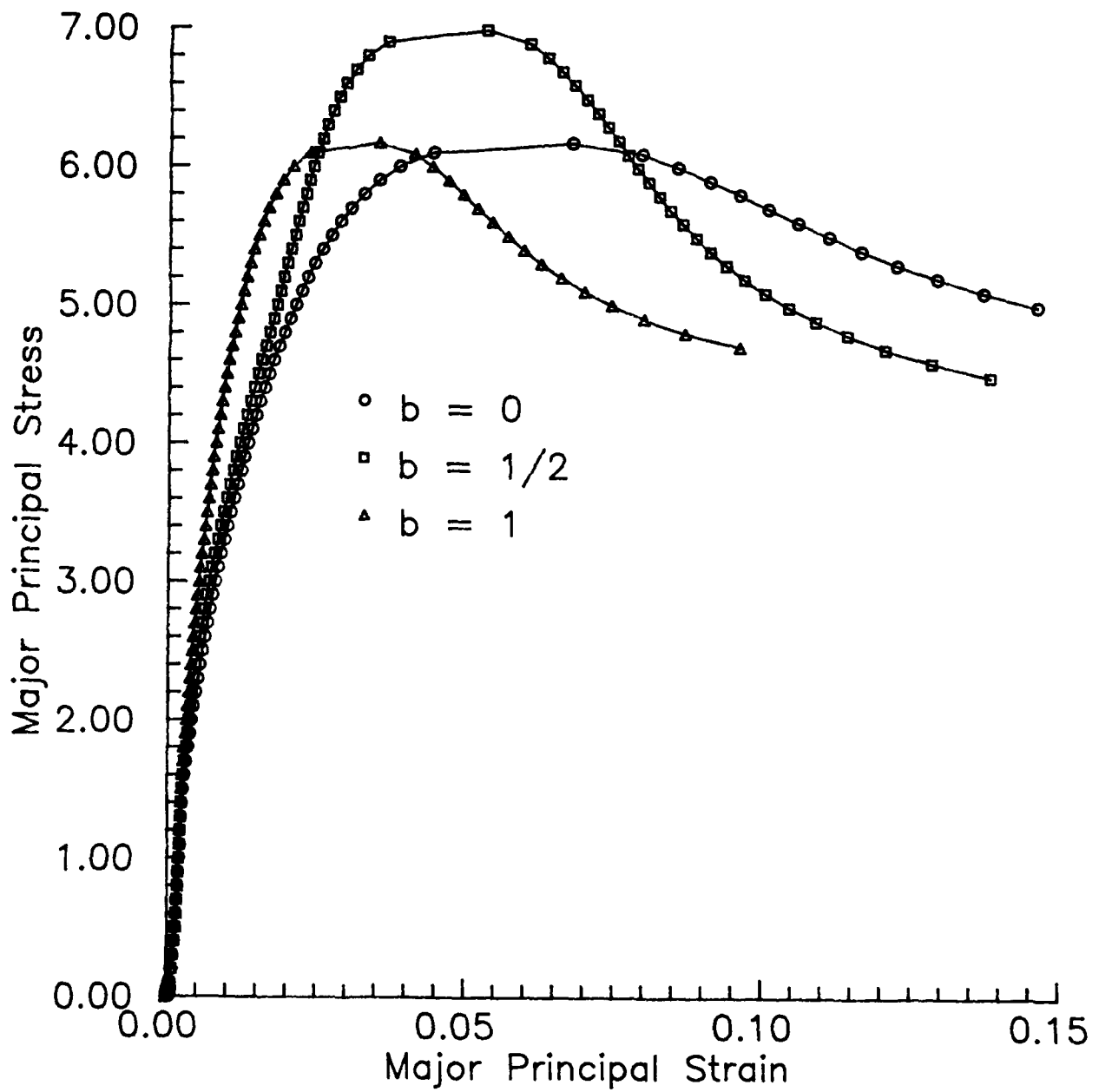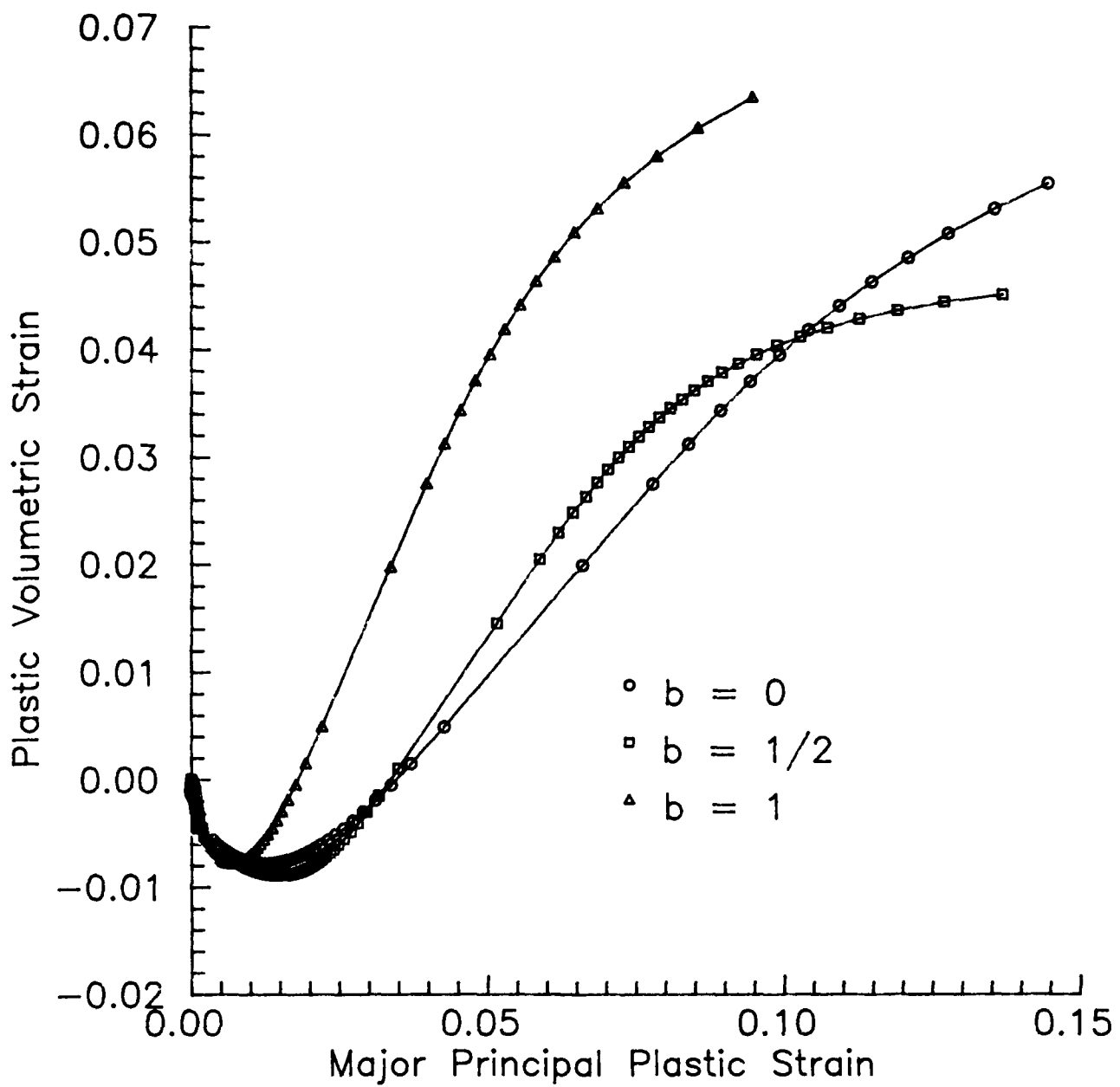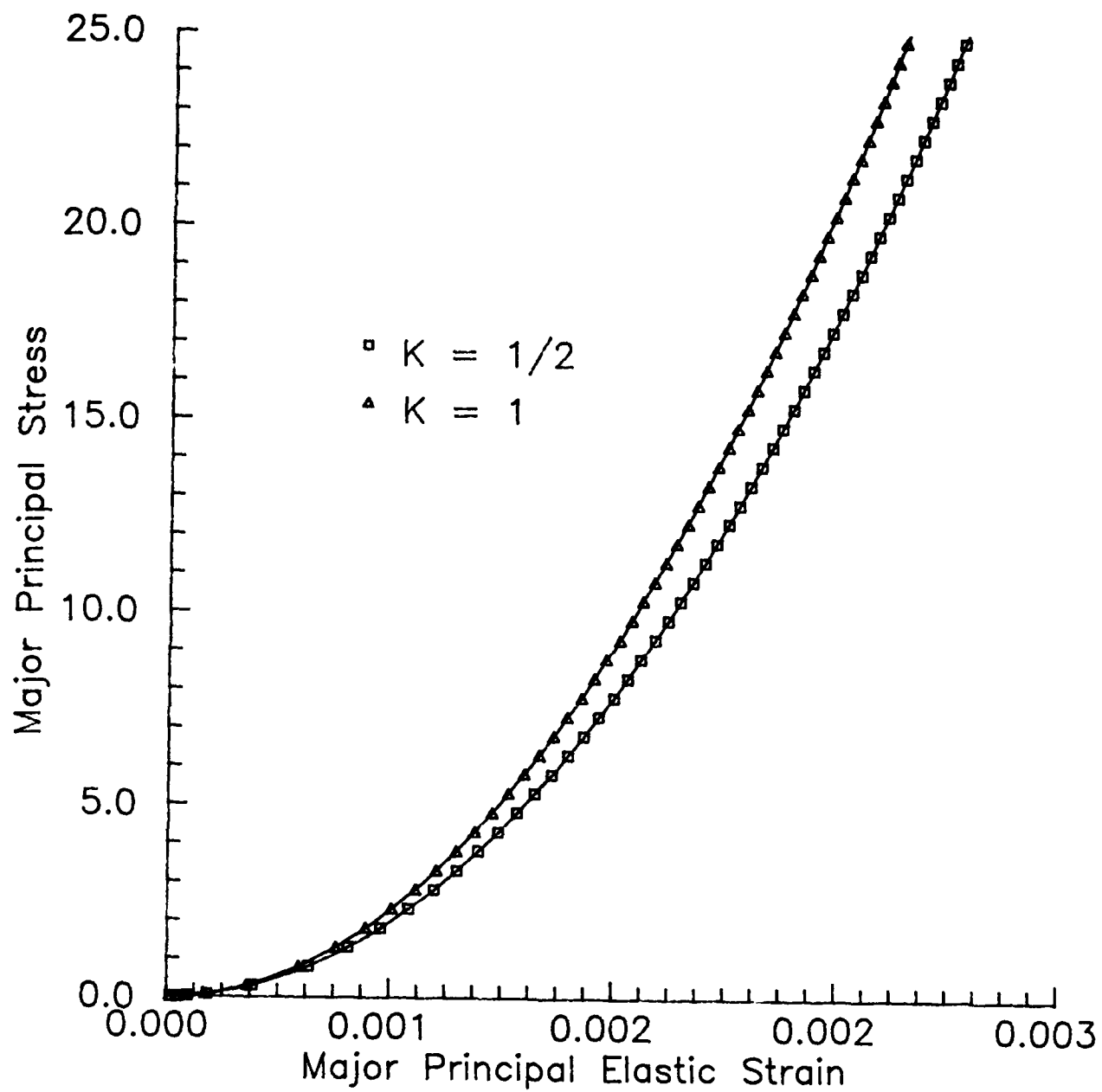Plastic Strain Results for Three Class
1 Loadings

Fig. 14. Elastic Stress-Strain Results for Two
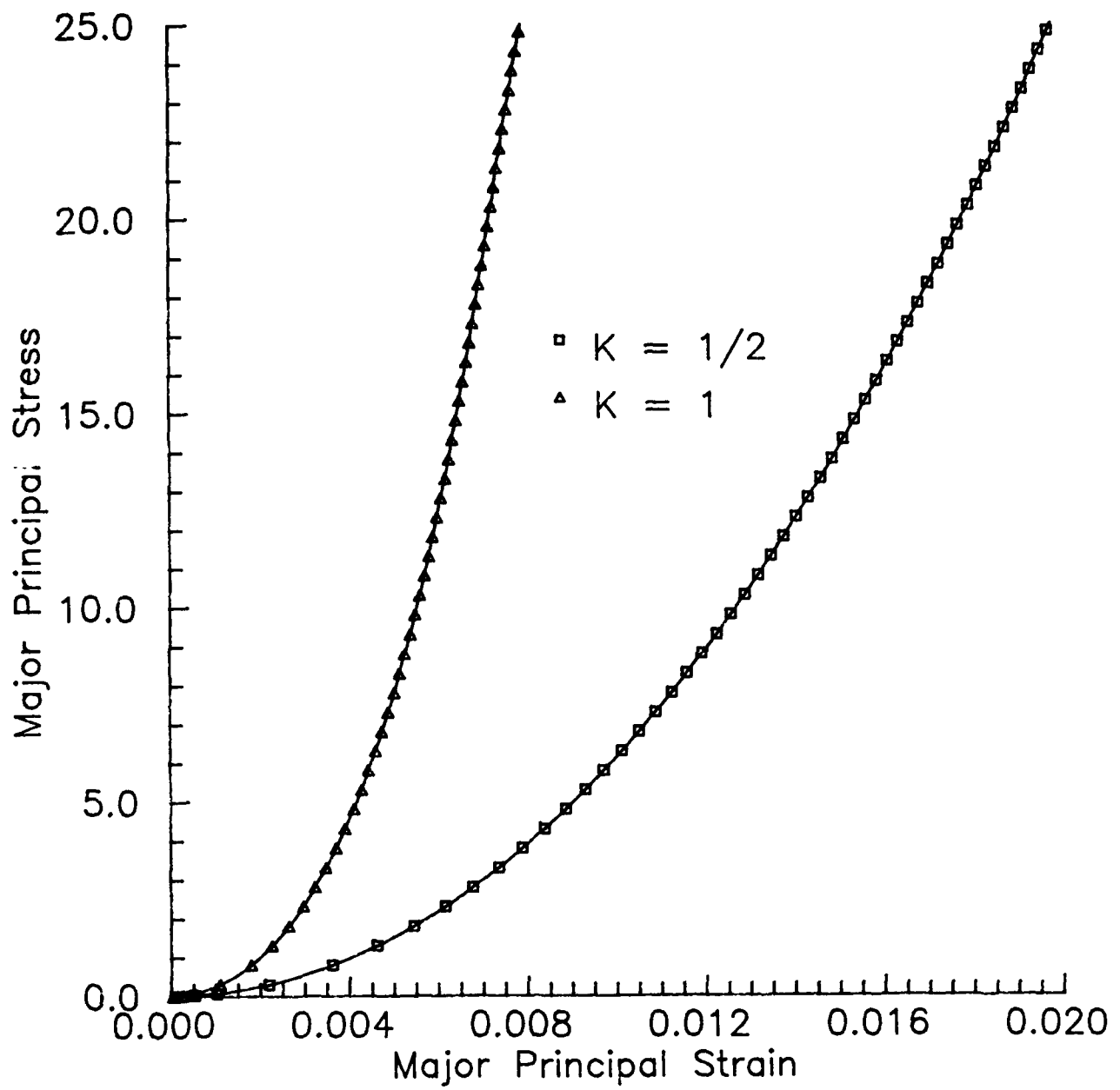Class 2 Loadings

Fig. 15.   Total Stress-Strain Results for Two
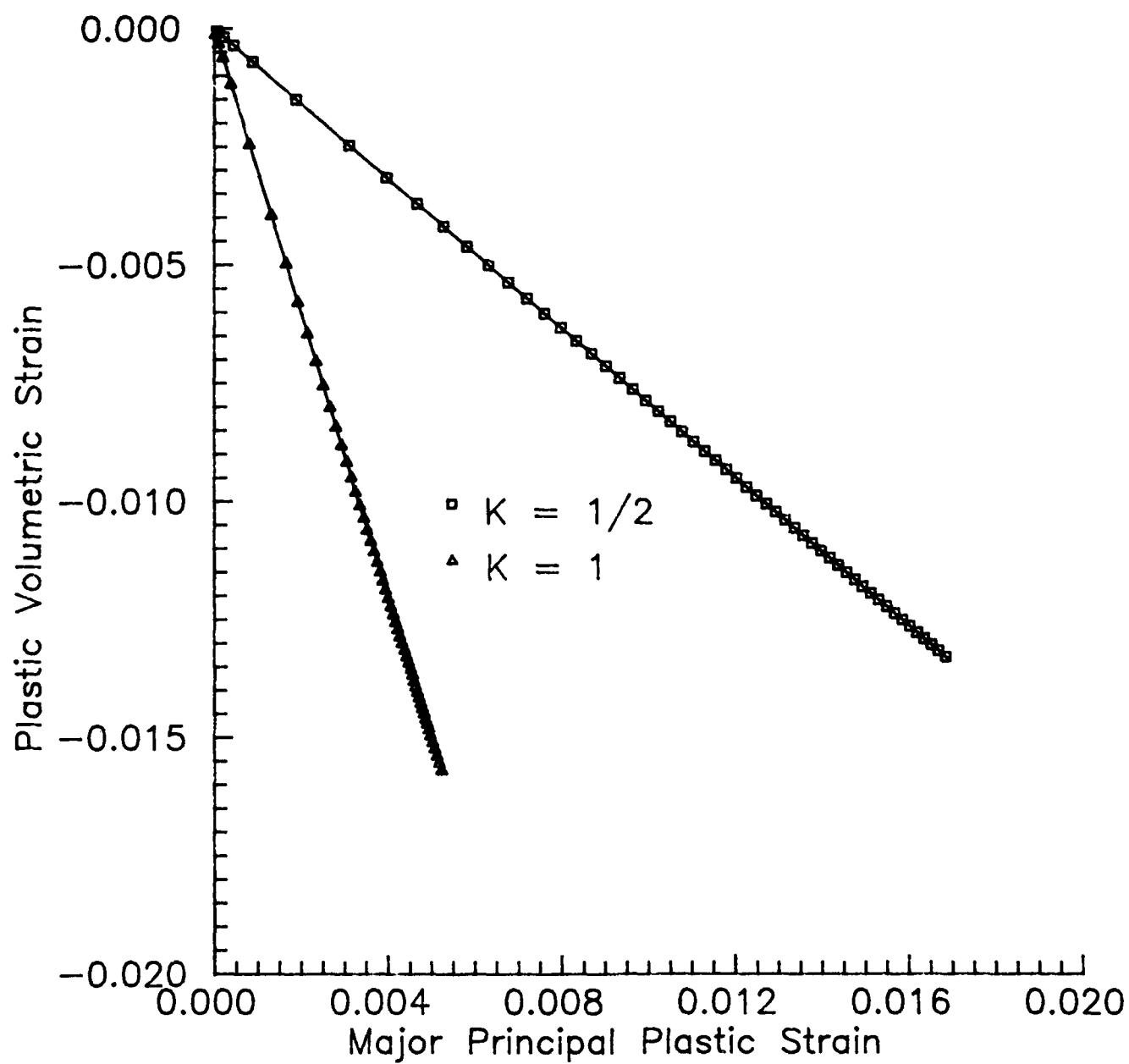Class 2 Loadings

Fig. 16. Negative Volumetric Plastic Strain –
Plastic Strain Results for Two Class
2 Loadings

SUMMARY

This report has presented the constitutive equations for solving three-dimensional elasto-plastic cohesionless soil problems for monotonic loading via the finite element method. The soil constitutive equations have been carefully constructed to incorporate the particulate nature of soils, i.e. kinematics of particle movement, particle crushing and particle contact bonding. Constitutive modeling of the elastic component is based on the Hertz and Mindlin theories, whereas the plastic component is formulated using stress-dilatancy theory. Since the constitutive equations have been developed utilizing small-strain data from wave propagation and vibration tests with data for large strains, the coefficients used in the constitutive equations are valid for a wide range of loading conditions.

The focus of this research effort has been to formulate soil constitutive equations that realistically represent the particulate behavior of soils. This is being achieved by using constitutive models that have coefficients that are physically understandable, are nearly constant for a wide variety of conditions, and includes initial efforts towards understanding the effects of sample disturbance on the coefficients. Combining the physically realistic soil constitutive equations being developed in this research with finite elements that accurately represent boundary conditions and displacement variations provides a method of analysis that has a good chance of predicting field performance.

RECOMMENDATIONS FOR FUTURE RESEARCH

Though a great deal has been achieved in understanding and quantifying the three-dimensional elasto-plastic behavior of soils, much work remains to be completed for the wide variety of problems encountered in geotechnical engineering. Some of the areas requiring additional investigation include: elasto-plastic cohesive soil behavior, cyclic loading behavior for both cohesionless and cohesive soils, rotation of principal stress and stress increments on the behavior of particulate materials, and inherent and stress induced plastic anisotropy.

Additional finite element work includes implementation and testing

of the constitutive equation developments and the utilization and verification of EPSAP for a variety of boundary value problems encountered in geotechnical engineering. This phase will also require modifying the constitutive equations for the special cases of plane strain and axisymmetric behavior. Furthermore, investigation and implementation of large strain behavior must still be completed. The use of the developed natural strain approach may not be computationally feasible for some soil static problems.

Another major activity which should be undertaken is the development of a computer simulation problem to investigate the behavior of particle packings. A preliminary effort in this regard has been completed during the current contract as outlined in the next section.

COMPUTER SIMULATION OF PARTICLE BEHAVIOR

When attempting to explain some types of soil behavior one may be led to speculate about the nature of particle movements within an element of deforming soil. Which contacts within the element are experiencing gross sliding at a given instant of deformatior.' What is the distribution of orientations of sliding contacts? Do groups of particles slide past one another, and if so, how many particles are in the sliding groups? Because it is difficult to observe the behavior of individual particles and contacts within a soil sample in the laboratory, it will apparently be instructive to simulate the behavior of a packing of particles with a computer model.

Aspects of soil behavior that invite questions about the nature of particle movements are: (1) the effect on soil deformation of a change in direction of the stress increment vector (rotation of stress increment); (2) the nature and development of inherent and stress-induced anisotropy in particulate materials; and (3) the effects of contact cohesion on soil deformation.

REFERENCES

1. Barlow, J. (1976), "Optimal Stress Locations in Finite Element Models," *International Journal for Numerical Methods in Engineering*, Vol. 10, pp. 243-251.

2. Bathe, K. J. and Cimento, A.P. (1980), "Some Practical Procedures for the Solution of Nonlinear Finite Element Equations," *Computer Methods in Applied Mechanics and Engineering*, Vol. 22, pp. 231-277.

3. Blandford, G. E. and Hardin, B. O. (1985), *Three-Dimensional Elasto-Plastic Analysis for Soils*, Air Force Office of Scientific Research, September, 170 pp.

4. Blandford, G. E. and Hardin, B. O. (1988), "3D Elasto-Plastic Finite Element Analysis of Cohesionless Soils," to be be submitted to *International Journal for Numerical and Analytical Methods in Geomechanics*.

5. Drucker, D. C., Gibson, R. E. and Henkel, D. J. (1957), "Soil Mechanics and Work-Hardening Theories of Plasticity," *Transactions*, ASCE, Vol. 122, pp. 338-446.

6. Hardin, B. O. (1978), "The Nature of Stress-Strain Behavior for Soils," *State-of-the-Art Report for the ASCE Specialty Conference on Earthquake Engineering and Soil Dynamics*, Pasadena, CA, Vol. 1, June, pp. 3-90.

7. Hardin, B. O. (1980), discussion of "Anisotropic Shear Modulus Due to Stress Anisotropy," *Journal of the Geotechnical Engineering Division*, ASCE, Vol. 106, No. GT8, pp. 956-958.

8. Hardin, B. O. (1985a), "Crushing of Soil Particles," *Journal of the Geotechnical Division*, ASCE, In press.

9. Hardin, B. O. (1985b), "Strength of Soils in Terms of Effective Stress," *Richart Commemorative Lectures*, ASCE, Detroit, MI, October.

10. Hardin, B. O. (1987), "1D Strain in Normally Consolidated Cohesionless Soils," *Journal of Geotechnical Engineering*, ASCE, Vol. 113, No. 12, pp. 1449 - 1467.

11. Hardin, B. O., Hardin, K. O. and Schwab, C. V. (1988), "Triaxial Compression, Simple Shear and Strength of Wheat," *1988 International Summer Meeting of the American Society of Agricultural Engineers*, Rapid City, SD, June 26-29, Paper #88-4022, 34 pp.; in review for possible publication in the *Transactions, ASAE*.

12. Hardin, B. O. (1988a), "1D Strain in Normally Consolidated Cohesive Soils," *Journal of Geotechnical Engineering*, ASCE, 39 pp., To be published.

13. Hardin, B. O. (1988b), "The Low-Stress Dilation Test," submitted to Journal of Geotechnical Engineering, ASCE, April 1988, 36 pp.

14. Hardin, B. O. (1988c), "Effect of Rigid Boundaries on Measurement of Particle Concentration," submitted to Journal of Geotechnical Engineering, ASCE, May, 1988, 17pp.

15. Hardin, B. O. (1988d), "Triaxial Compression for Cohesionless Soils," to be submitted to Journal of Geotechnical Engineering, ASCE.

16. Hardin, B. O. and Blandford, G. E. (1986), "Three-Dimensional Elasto-Plastic Analysis for Soils," second annual report to AFOSR, Sep., 150 pp.

17. Hardin, B. O. and Blandford, G. E. (1987), "Three-Dimensional Elasto-Plastic Analysis for Soils," third annual report to AFOSR, Sep., 150 pp.

18. Hardin, B. O. and Blandford, G. E. (1988a), "Elasticity for Particulate Materials," submitted to Journal of Geotechnical Engineering, ASCE, August 1988, 34 pp.

19. Hardin, B. O. and Blandford, G. E. (1988b), "3D Constitutive Equations for Cohesionless Soils," to be submitted to Journal of Geotechnical Engineering, ASCE.

20. Hsu, T. R. (1986). The Finite Element Method in Thermomechanics, Allen and Unwin, Boston, MA.

21. Hughes, T. J. R. (1987). The Finite Element Method - Linear Static and Dynamic Finite Element Analysis, Prentice-Hall, Englewood Cliffs, NJ.

22. Key, S. W., Stone, C. M. and Krieg, R. D. (1981), "Dynamic Relaxation Applied to the Quasi-Static, Large Deformation, Inelastic Response of Axisymmetric Structures," Non-Linear Finite Element Analysis in Structural Mechanics, W. Wunderlich, E. Stein and K. J. Bathe (Editors), Springer-Verlag, New York, pp. 585-620.

23. Koerner, R. M. (1968), "The Behavior of Cohesionless Soils Formed from Various Minerals," Soil Mechanics Series No. 16, School of Engineering, Duke University, 305 pp.

24. Marques, J. M. M. C. and Owen, D. R. J. (1984), "Infinite Elements in Quasi-Static Material Nonlinear Problems," Computers and Structures, Vol. 18, No. 4, pp. 739-751.

25. Ramm, E. (1981), "Strategies for Tracing Non-Linear Responses Near Limit Points," Non-Linear Finite Element Analysis in Structural Mechanics, W. Wunderlich, E. Stein and K. J. Bathe (Editors), Springer-Verlag, New York, pp. 63-89.

26. Roesler, S. K. (1979), "Anisotropic Shear Modulus Due to Stress Anisotropy," _Journal of the Geotechnical Engineering Division_, ASCE, Vol. 105, No. GT7, Jul., pp. 871-880.

27. Rowe, P. W. (1962), "The Stress-Dilatancy Relation for Static Equilibrium of an Assembly of Particles in Contact," _Proceedings of the Royal Society of London_, Series A, Vol. 269, pp. 500-527.

28. Rowe, P. W. (1971), "Theoretical Meaning and Observed Values of Deformation Parameters for Soils," _Proceedings of the Roscoe Memorial Symposium on Stress-Strain Behavior of Soils_, March, pp. 143-194.

29. Schofield, A. and Wroth, P. (1968), _Critical State Soil Mechanics_, McGraw-Hill, New York, NY.

30. Taylor, R. L., Beresford, P. J. and Wilson, E. L. (1976), "A Non-Conforming Element for Stress Analysis," _International Journal for Numerical Methods in Engineering_, Vol. 10, pp. 1211-1219.

31. Taylor, R. L. (1977), "Computer Procedures for Finite Element Analysis," in O. C. Zienkiewicz, _The Finite Element Method_, Third Edition, Chapter 24.

32. Washizu, K. (1968). _Variational Methods in Elasticity and Plasticity_, Pergamon Press, NY.

33. Wilson, E. L., Taylor, R. L., Doherty, W. P., and Ghaboussi, J. (1973), "Incompatible Displacement Models," _Numerical and Computer Methods in Structural Mechanics_, S. J. Fenves, N. Perrone, A. R. Robinson, and W. C. Schnobrich (Editors), Academic Press, New York, pp. 43 57.

34. Zienkiewicz, O. C. (1977), _The Finite Elment Method_, Third Edition, McGraw-Hill, New York, NY.

35. Zienkiewicz, O. C., Bettess, P., Chiam, T. C. and Emson, C. (1981), "Numerical Methods for Unbounded Field Problems and a New Infinite Element Formulation," _Winter Annual Meeting - Applied Mechanics Division_, Washington, D.C., pp. 115-148.

36. Zienkiewicz, O. C., Emson, C. and Bettess, P. (1983), "A Novel Boundary Infinite Element," _International Journal for Numerical Methods in Engineering_, Vol. 19, pp. 393-404.

APPENDIX I

FINITE ELEMENT FORMULATION DETAILS

FINITE ELEMENT FORMULATION DETAILS

The purpose of this appendix is to present the finite element formulation details associated with the three-dimensional computer program EPSAP (Elasto-Plastic Soil Analysis Program). These formulation details include: (1) element shape functions and shape function matrices (which includes the element strain-displacement matrices) for the finite elements shown in Fig. 5, (2) curvilinear coordinate transformations for the isoparametric implementation, (3) numerical integration and (4) stress and strain calculations.

Element Shape Functions and Shape Function Matrices

Shape functions for the elements of Fig. 5 and the shape functions matrices are explicitly given in this section. First, the shape functions corresponding the the line load element of Fig. 5a are

$$N_1^\ell = (1 - \zeta)/2$$

$$N_2^\ell = (1 + \zeta)/2$$

(A1)

where $-1 \leq \zeta \leq 1$ is the nondimensionalized local coordinate shown in Fig. 5a and subscript i (i=1,2) corresponds to the two element node points. The matrix of line element shape functions, $[N^\ell]$, is defined as

$$[N^\ell] = \begin{bmatrix} N_1^\ell & 0 & 0 & N_2^\ell & 0 & 0 \\ 0 & N_1^\ell & 0 & 0 & N_2^\ell & 0 \\ 0 & 0 & N_1^\ell & 0 & 0 & N_2^\ell \end{bmatrix}$$

(A2)

Equation A2 shows that $[N^\ell]$ is composed of the two basic shape functions (Eq. A1), the positioning of the shape functions being dictated by the nodal x-, y- and z-axis line traction values. The line tractions are approximated as

$$\left\{\begin{array}{c} t_x^\ell \\ t_y^\ell \\ t_z^\ell \end{array}\right\} = \left[\begin{array}{ccc} N_i^\ell & 0 & 0 \\ 0 & N_i^\ell & 0 \\ 0 & 0 & N_i^\ell \end{array}\right] \left\{\begin{array}{c} t_{xi}^\ell \\ t_{yi}^\ell \\ t_{zi}^\ell \end{array}\right\} \tag{A3}$$

where summation on the repeated subscripts is implied and t_{xi}^ℓ, t_{yi}^ℓ, t_{zi}^ℓ are the nodal line traction values.

The four node quadrilateral element (Fig. 5b) shape functions are (e.g. Zienkiewicz, 1977)

$$N_i^S = \frac{1}{4} (1 + \xi_0) (1 + \eta_0) \; ; \quad i=1,2,3,4 \tag{A4}$$

in which $-1 \leq \xi, \eta \leq 1$ are normalized curvilinear coordinates (see Fig. 5b), $\xi_0 = \xi_i \xi$, $\eta_0 = \eta_i \eta$, and ξ_i, η_i are ± 1 depending on node location i, e.g. $\xi_i = -1$ for $i=1,4$ and $\eta_i = 1$ for $i=3,4$.

The matrix of surface element shape functions, $[N^S]$, is defined to be

$$[N^S] = \left[\begin{array}{ccc} N_i^S & 0 & 0 \\ 0 & N_i^S & 0 \\ 0 & 0 & N_i^S \end{array}\right] \tag{A5}$$

in which the pattern of Eq. A5 is repeated for $i=1,2,3,4$. The surface tractions $\{t^S\}$ are interpolated in the same manner as the line element tractions i.e.

$$\left\{\begin{array}{c} t_x^S \\ t_y^S \\ t_z^S \end{array}\right\} = \left[\begin{array}{ccc} N_i^S & 0 & 0 \\ 0 & N_i^S & 0 \\ 0 & 0 & N_i^S \end{array}\right] \left\{\begin{array}{c} t_{xi}^S \\ t_{yi}^S \\ t_{zi}^S \end{array}\right\} \tag{A6}$$

where summation on the repeated subscripts is implied and t_{xi}^S, t_{yi}^S, t_{zi}^S are the nodal surface traction values.

The element shape functions for the basic eight node hexahedron element (Fig. 5c) are (e.g. Zienkiewicz, 1977)

$$N_i = \frac{1}{8} (1 + \zeta_0)(1 + \eta_0)(1 + \zeta_0) \quad ; \quad i=1,2,\ldots,8 \qquad \text{(A7)}$$

where $\zeta_0 = \zeta_i \zeta$ and $-1 \leq \zeta \leq 1$ ($\xi_i = 1$ for $i=2,3,6,7$; $\eta_i = 1$ for $i = 3,4,$ 7,8; $\zeta_i = 1$ for $i=5,6,7,8$). These basic eight node hexahedron element shape functions are used to describe the element geometry and the volume element shape function matrix, $[N]$. Similar to the line and surface element shape function matrices, the volume element shape function matrix is defined as

$$[N] = \begin{bmatrix} N_i & 0 & 0 \\ 0 & N_i & 0 \\ 0 & 0 & N_i \end{bmatrix} \qquad \text{(A8)}$$

where $i=1,2,\ldots,8$.

A disadvantage of the volume element shape functions represented by Eq. A7 is that they cannot represent general linear stress variations. Wilson et al. (1973) proposed that the incompatible "bubble mode" functions:

$$N_1^b = (1 - \xi^2)$$

$$N_2^b = (1 - \eta^2) \qquad \text{(A9)}$$

$$N_3^b = (1 - \zeta^2)$$

which are zero at all eight node points be added to element displacement approximation in order to represent linear stress variations. The addition of the bubble mode shape functions leads to the following element displacement variations:

$$u = N_i u_i + N_j^b a_x^j$$

$$v = N_i v_i + N_j^b a_y^j \qquad \text{(A10)}$$

$$w = N_i w_i + N_j^b a_z^j$$

where u, v, w are the x-axis, y-axis and z-axis displacements, respectively; u_i, v_i, w_i are the standard node point displacements; and a_x^j,

3

a_y^j, a_z^j (j=1,2,3) are additional degrees of freedom associated with the internal bubble mode shape functions. Utilizing the displacement approximations of Eq. A10 results in a modified eight node hexahedron element.

Equation A10 shows that the number of displacement variables for the modified eight node hexahedron is 33 rather than the usual 24. Elimination of the additional nine variables (a_x^j, a_y^j a_z^j; j=1,2,3) is accomplished using static condensation on the element stiffness matrix. Before pursuing static condensation, generation of the element strain-displacement matrix for the modified eight node hexahedron element will be presented.

The element strain-displacement matrix is obtained by first defining the incremental strain-displacement relationships:

$$
\begin{Bmatrix} d\epsilon_x \\ d\epsilon_y \\ d\epsilon_z \\ d\gamma_{xy} \\ d\gamma_{yz} \\ d\gamma_{zx} \end{Bmatrix} = \begin{bmatrix} -\frac{\partial}{\partial x} & 0 & 0 \\ 0 & -\frac{\partial}{\partial y} & 0 \\ 0 & 0 & -\frac{\partial}{\partial z} \\ \frac{\partial}{\partial y} & \frac{\partial}{\partial x} & 0 \\ 0 & \frac{\partial}{\partial z} & \frac{\partial}{\partial y} \\ \frac{\partial}{\partial z} & 0 & \frac{\partial}{\partial x} \end{bmatrix} \begin{Bmatrix} du \\ dv \\ dw \end{Bmatrix}
\qquad (A11)
$$

where the negative sign for the direct strain increments is used since compressive strains are positive. Substituting the displacement variations of Eq. A10 into Eq. A11 results in

4

$$
\begin{Bmatrix} d\epsilon_x \\ d\epsilon_y \\ d\epsilon_z \\ d\gamma_{xy} \\ d\gamma_{yz} \\ d\gamma_{zx} \end{Bmatrix} = \begin{bmatrix} -\partial N_i/\partial x & 0 & 0 \\ 0 & -\partial N_i/\partial y & 0 \\ 0 & 0 & -\partial N_i/\partial z \\ \partial N_i/\partial y & \partial N_i/\partial x & 0 \\ 0 & \partial N_i/\partial z & \partial N_i/\partial y \\ \partial N_i/\partial z & 0 & \partial N_i/\partial x \end{bmatrix} \begin{Bmatrix} du_i \\ dv_i \\ dw_i \end{Bmatrix}
$$

$$
+ \begin{bmatrix} -\partial N_j^b/\partial x & 0 & 0 \\ 0 & -\partial N_j^b/\partial y & 0 \\ 0 & 0 & -\partial N_j^b/\partial z \\ \partial N_j^b/\partial y & \partial N_j^b/\partial x & 0 \\ 0 & \partial N_j^b/\partial z & \partial N_j^b/\partial y \\ \partial N_j^b/\partial z & 0 & \partial N_j^b/\partial x \end{bmatrix} \begin{Bmatrix} da_x^j \\ da_y^j \\ da_z^j \end{Bmatrix}
$$

or

$$
\{d\epsilon\} = [B^H] \{dp^e\} + [B^B] \{da\} \tag{A12}
$$

where $[B^H]$ is the strain-displacement matrix associated with the element node point displacements $\{p^e\}$ and $[B^B]$ is the strain-displacement matrix corresponding the the bubble mode displacement variables $\{a\}$.

The element elastic stiffness matrix is constructed as

$$
[k_E] = \int_{\Omega_e} [B]^T [C_E] [B] \, d\Omega
$$

$$
= \int_{\Omega_e} \left[\begin{array}{c} [B^H]^T \\ \hline [B^B]^T \end{array} \right] [C_E] \left[\; [B^H] \; | \; [B^B] \; \right] \; d\Omega
$$

$$
= \int_{\Omega_e} \left[\begin{array}{c|c} [B^H]^T [C_E] [B^H] & [B^H]^T [C_E] [B^B] \\ \hline [B^B]^T [C_E] [B^H] & [B^B]^T [C_E] [B^B] \end{array} \right] \; d\Omega
$$

$$
= \left[\begin{array}{c|c}
[k_E^{HH}] & [k_E^{HB}] \\
\hline
[k_E^{BH}] & [k_E^{BB}]
\end{array} \right] \tag{A13}
$$

where $[B] = [\ [B^H]\ |\ [B^B]\ ]$ is the element strain-displacement matrix.

Static condensation of the element elastic stiffness matrix is obtained by eliminating the incremental bubble mode displacement parameters from

$$
\left[\begin{array}{c|c}
[k_E^{HH}] & [k_E^{HB}] \\
\hline
[k_E^{BH}] & [k_E^{BB}]
\end{array} \right]
\left\{ \begin{array}{c}
\{dp^e\} \\
\hline
\{da\}
\end{array} \right\}
=
\left\{ \begin{array}{c}
\{df\} \\
\hline
\{0\}
\end{array} \right\} \tag{A14}
$$

Expanding the lower partition of Eq. A14 results in

$$
[k_E^{BH}]\ \{dp^e\}\ +\ [k_E^{BB}]\ \{da\}\ =\ \{0\}
$$

$$
\{da\}\ =\ -\ [k_E^{BB}]^{-1}\ [k_E^{BH}]\ \{dp^e\} \tag{A15}
$$

Substituting Eq. A15 into the upper partition of Eq. A14 leads to

$$
[\ [k_E^{HH}]\ -\ [k_E^{HB}]\ [k_E^{BB}]^{-1}\ [k_E^{BH}]\ ]\ \{dp^e\}\ =\ \{df\}
$$

$$
[\bar{k}_E\ ]\ \{dp^e\}\ =\ \{df\} \tag{A16}
$$

Equation A16 defines the statically condensed elastic stiffness matrix.

A problem with the formulation given by Eq. A13 is that the modified hexahedron element does not pass the patch test unless the element geometry is at least a parallelpiped. Lack of satisfying the patch test may lead to erroneous results. Taylor et al. (1976) designed a "repair" for the two-dimensional version of the element such that for an arbitrary element geometry the modified element will pass the patch test. Their repair involves calculating the bubble mode strain-displacement matrix using the centroidal (i.e. $\xi = \eta = \zeta = 0$) evaluation of the Jacobian matrix and Jacobian determinant. Further details of this calculation are presented in the curvilinear coordinate transformations

and numerical intergration sections.

The infinite element shown in Fig. 5d is taken from Marques and Owen (1984) and is based on the mapped infinite element concept of Zienkiewicz et al. (1981, 1983). Mapped infinite elements are based on a simple mapping technique that applies to both modelling of the geometry and the field variable (e.g. displacements in stress analysis).

The concept underlying mapped infinite elements is most easily understood in the context of the one-dimensional element shown in Fig. A.1. Nodes 1, 2 and 3 (node 3 is at infinity) of Fig. A.1a are mapped onto the parent element defined by the local coordinate system $-1 \leq \xi \leq 1$ as shown in Fig. A.1b. The pole (i.e. point of singularity for the mapping) position labelled 0 in Fig. A.1a is arbitrary (though its position influences the accuracy of the results) and $x_0 \leq x_1$. Once x_0 is chosen, the location of node 2 is defined by

$$x_2 = 2x_1 - x_0 \tag{A17}$$

Interpolation between the local and global coordinate systems is

$$x(\xi) = \sum_{i=1}^{2} M_i(\xi) \, x_i \tag{A18}$$

where the summation extends over the finite nodes only and the mapping functions M_i are given by

$$M_1 = -2\xi/(1 - \xi)$$
$$M_2 = (1 + \xi)/(1 - \xi) \tag{A19}$$

Examining Eq. A19 shows that for $\xi = -1, 0, 1$ the corresponding x-coordinates are x_1, x_2, ∞.

Interpolation for the x-axis displacement uses standard Lagrangian approximations to give

$$u = \sum_{i=1}^{3} N_i \, u_i = 0.5\xi(\xi-1) \, u_1 + (1-\xi^2) \, u_2 + 0.5\xi(\xi+1) \, u_3 \tag{A20}$$

Solving Eq. A18 for ξ leads to

$$\xi = 1 - 2a/r \tag{A21}$$

in which r denotes the distance from the pole to a general point within the element and a = x_2 - x_1 as shown in Fig. A.1a. Substituting Eq. A21 into Eq. A20 results in

$$u = u_3 + (-u_1 + 4u_2 - 3u_3) \, a/r + (2u_1 - 4u_2 + 2u_3) \, (a/r)^2 \quad \text{(A22)}$$

Thus, as r tends to infinity, u approaches u_3 which is assumed to be zero in the present implementation. Consequently, summation over the finite nodes is all that is required in formulating the finite element equations. Equation A22 also clearly shows the role of the pole position, 0.

The mapping and displacement shape functions corresponding to the eight node isoparametric element of Fig. 5d are (Marques and Owen, 1984)

$$M_i = \frac{1}{2} (1 + \xi_0) (1 + \eta_0) (-\zeta)/(1 - \zeta) \; ; \; i=1,2,3,4$$

$$M_i = \frac{1}{4} (1 + \xi_0) (1 + \eta_0) (1 + \zeta)/(1 - \zeta) \; ; \; i=5,6,7,8$$

(A23)

$$N_i = \frac{1}{8} (1 + \xi_0) (1 + \eta_0) (\zeta^2 - \zeta) \; ; \; i=1,2,3,4$$

$$N_i = \frac{1}{4} (1 + \xi_0) (1 + \eta_0) (1 - \zeta^2) \; ; \; i=5,6,7,8$$

(A24)

Equations A23 and A24 show that the eight node isoparmetric infinite element uses a bilinear approximation in the finite ξ - η plane and a quadratic decay in the infinite ζ-direction.

The infinite element strain-displacement matrix is obtained by substituting the shape functions of Eq. A24 into the incremental strain-displacement relationships of Eq. A11 which results in

$$[B] = \begin{bmatrix} -\partial N_i/\partial x & 0 & 0 \\ 0 & -\partial N_i/\partial y & 0 \\ 0 & 0 & -\partial N_i/\partial z \\ \partial N_i/\partial y & \partial N_i/\partial x & 0 \\ 0 & \partial N_i/\partial z & \partial N_i/\partial y \\ \partial N_i/\partial z & 0 & \partial N_i/\partial x \end{bmatrix} \qquad (A25)$$

The infinite element elastic stiffness matrix is obtained by substituting Eq. A25 into

$$[k_E] = \int_{\Omega_e} [B]^T [C_E] [B] \, d\Omega$$

Curvilinear Coordinate Transformations

The element matrices and integrals of the previous section involve global coordinates whereas all the shape functions have been expressed in terms of local coordinates on the appropriate parent elements. Consequently, a transformation of coordinates between the global and local coordinate systems is required to formulate the element stiffness matrices and load vectors. These transformations are obtained using isoparametric finite element transformation procedures which are described in this section.

Basically, an isoparametric finite element formulation involves approximating the finite element geometry (represented by shape functions M_i) in the same manner as the element displacement variations in terms of the node point displacements (represented by shape functions N_i), i.e. set $M_i = N_i$ except for the infinite element of Fig. 5d in which case the special geometric interpolation functions of Eq. A23 are used. Details of the various transformations required in EPSAP are presented in the following paragraphs.

The elements used in EPSAP require the evaluation of the arc length transformation

$$d\Gamma_\ell = J_\Gamma^\ell(\xi) \, d\xi \qquad (A26)$$

where $J_\Gamma^\ell(\xi)$ is the arc length Jacobian, the surface area transformation

9

$$d\Gamma_s = J_\Gamma^s(\xi,\eta) \, d\xi \, d\eta \qquad (A27)$$

where $J_\Gamma^s(\xi,\eta)$ is the surface area Jacobian, the volume transformation

$$d\Omega = |J(\xi,\eta,\zeta)| \, d\xi \, d\eta \, d\zeta \qquad (A28)$$

where $|J(\xi,\eta,\zeta)|$ is the three-dimensional Jacobian determinant, as well as volume shape function derivatives with respect to x, y and z as shown in Eqs. A12 and A25.

The arc length Jacobian of Eq. A26 is

$$J_\Gamma^\ell(\xi) = \sqrt{\left(\frac{\partial x}{\partial \xi}\right)^2 + \left(\frac{\partial y}{\partial \xi}\right)^2 + \left(\frac{\partial z}{\partial \xi}\right)^2} \qquad (A29)$$

The finite element representation of Eq. A29 is obtained by substituting

$$x = \lfloor M^\ell \rfloor \{x\}$$

$$y = \lfloor M^\ell \rfloor \{y\}$$

$$z = \lfloor M^\ell \rfloor \{z\}$$

into Eq. A29 which results in

$$J_\Gamma^\ell(\xi) = \sqrt{\left[\frac{d\lfloor M^\ell \rfloor}{d\xi} \{x\}\right]^2 + \left[\frac{d\lfloor M^\ell \rfloor}{d\xi} \{y\}\right]^2 + \left[\frac{d\lfloor M^\ell \rfloor}{d\xi} \{z\}\right]^2}$$

$$\cdots \quad (A30)$$

where $\lfloor M^\ell \rfloor = \lfloor N^\ell \rfloor$ is the row vector of line element shape functions (Eq. A1) and $\{x\}$, $\{y\}$, $\{z\}$ are the column vectors of element node point coordinates. The arc length transformation results in the limits of integration being $-1 \leq \xi \leq 1$.

The surface area transformation of Eq. A27 is

$$J_\Gamma^s(\xi,\eta) = \sqrt{\left(\frac{\partial x}{\partial \xi}\frac{\partial y}{\partial \eta} - \frac{\partial x}{\partial \eta}\frac{\partial y}{\partial \xi}\right)^2 + \left(\frac{\partial y}{\partial \xi}\frac{\partial z}{\partial \eta} - \frac{\partial y}{\partial \eta}\frac{\partial z}{\partial \xi}\right)^2 + \left(\frac{\partial z}{\partial \xi}\frac{\partial x}{\partial \eta} - \frac{\partial z}{\partial \eta}\frac{\partial x}{\partial \xi}\right)^2}$$

$$\cdots \quad (A31)$$

and the finite element form is obtained by substituting

$$x = \lfloor M^s \rfloor \{x\}$$

$$y = \lfloor M^s \rfloor \{y\}$$

$$z = \lfloor M^s \rfloor \{z\}$$

into Eq. A31; $\lfloor M^s \rfloor = \lfloor N^s \rfloor$ is the row vector of surface element shape functions given in Eq. A4; and the other symbols are as previously defined.

The evaluation of the element volume integrals require not only the volume transformation, but also requires the evaluation of x, y and z coordinate derivatives as shown in the strain-displacement matrices of Eq. A12 and A25. Since the shape functions are expressed in terms of the nondimensionalized ξ, η and ζ coordinates; the x, y and z coordinate derivatives must be related to the ξ, η, ζ coordinate system. Using the chain rule of differentiation

$$\frac{\partial N_i}{\partial \xi} = \frac{\partial x}{\partial \xi}\frac{\partial N_i}{\partial x} + \frac{\partial y}{\partial \xi}\frac{\partial N_i}{\partial y} + \frac{\partial z}{\partial \xi}\frac{\partial N_i}{\partial z}$$

$$\frac{\partial N_i}{\partial \eta} = \frac{\partial x}{\partial \eta}\frac{\partial N_i}{\partial x} + \frac{\partial y}{\partial \eta}\frac{\partial N_i}{\partial y} + \frac{\partial z}{\partial \eta}\frac{\partial N_i}{\partial z} \qquad \text{(A32)}$$

$$\frac{\partial N_i}{\partial \zeta} = \frac{\partial x}{\partial \zeta}\frac{\partial N_i}{\partial x} + \frac{\partial y}{\partial \zeta}\frac{\partial N_i}{\partial y} + \frac{\partial z}{\partial \zeta}\frac{\partial N_i}{\partial z}$$

where N_i are the shape functions given in Eq. A7 or A24. Writing Eq. A32 in matrix form results in

$$\left\{ \begin{array}{c} \dfrac{\partial N_i}{\partial \xi} \\[2ex] \dfrac{\partial N_i}{\partial \eta} \\[2ex] \dfrac{\partial N_i}{\partial \zeta} \end{array} \right\} = \left[\begin{array}{ccc} \dfrac{\partial x}{\partial \xi} & \dfrac{\partial y}{\partial \xi} & \dfrac{\partial z}{\partial \xi} \\[2ex] \dfrac{\partial x}{\partial \eta} & \dfrac{\partial y}{\partial \eta} & \dfrac{\partial z}{\partial \eta} \\[2ex] \dfrac{\partial x}{\partial \zeta} & \dfrac{\partial y}{\partial \zeta} & \dfrac{\partial z}{\partial \zeta} \end{array} \right] \left\{ \begin{array}{c} \dfrac{\partial N_i}{\partial x} \\[2ex] \dfrac{\partial N_i}{\partial y} \\[2ex] \dfrac{\partial N_i}{\partial z} \end{array} \right\} = [J] \left\{ \begin{array}{c} \dfrac{\partial N_i}{\partial x} \\[2ex] \dfrac{\partial N_i}{\partial y} \\[2ex] \dfrac{\partial N_i}{\partial z} \end{array} \right\} \qquad \text{(A33)}$$

where [J] is the Jacobian matrix. The shape function derivatives with respect to x, y and z can be obtained from Eq. A33 by premultiplying both sides by the inverse Jacobian matrix, $[J]^{-1}$, i.e.

$$
\left\{ \begin{array}{c} \dfrac{\partial N_i}{\partial x} \\[2mm] \dfrac{\partial N_i}{\partial y} \\[2mm] \dfrac{\partial N_i}{\partial z} \end{array} \right\} \;=\; [J]^{-1} \left\{ \begin{array}{c} \dfrac{\partial N_i}{\partial \xi} \\[2mm] \dfrac{\partial N_i}{\partial \eta} \\[2mm] \dfrac{\partial N_i}{\partial \zeta} \end{array} \right\}
\tag{A34}
$$

Since the ξ, η and ζ shape function derivatives are straightforward, Eq. A33 provides the partial derivatives of the shape functions with respect to x, y and z.

The Jacobian matrix of Eq. A33 is more explicitly expressed as

$$
[J] \;=\; \left[\begin{array}{ccc} \dfrac{\partial \lfloor M \rfloor}{\partial \xi}\{x\} & \dfrac{\partial \lfloor M \rfloor}{\partial \xi}\{y\} & \dfrac{\partial \lfloor M \rfloor}{\partial \xi}\{z\} \\[3mm] \dfrac{\partial \lfloor M \rfloor}{\partial \eta}\{x\} & \dfrac{\partial \lfloor M \rfloor}{\partial \eta}\{y\} & \dfrac{\partial \lfloor M \rfloor}{\partial \eta}\{z\} \\[3mm] \dfrac{\partial \lfloor M \rfloor}{\partial \zeta}\{x\} & \dfrac{\partial \lfloor M \rfloor}{\partial \zeta}\{y\} & \dfrac{\partial \lfloor M \rfloor}{\partial \zeta}\{z\} \end{array} \right] \;=\; \left[\begin{array}{ccc} J_{11} & J_{12} & J_{13} \\[3mm] J_{21} & J_{22} & J_{23} \\[3mm] J_{31} & J_{32} & J_{33} \end{array} \right]
$$

$$\cdots \tag{A35}$$

where $\lfloor M \rfloor = \lfloor N \rfloor$ for the modified eight node hexahedron element (see Eq. A7) and $\lfloor M \rfloor$ is the row vector of mapping functions given in Eq. A23 for the isoparametric eight node inifinte element. The Jacobian determinant and inverse Jacobian matrix are

$$
|J(\xi,\eta,\zeta)| \;=\; J_{11}(J_{22}J_{33} - J_{23}J_{32}) + J_{12}(J_{23}J_{31} - J_{21}J_{32})
$$
$$
+ \; J_{13}(J_{23}J_{31} - J_{22}J_{31})
\tag{A36}
$$

$$
[J]^{-1} \;=\; \frac{1}{|J|} \left[\begin{array}{ccc} J_{22}J_{33} - J_{23}J_{32} & J_{32}J_{13} - J_{12}J_{33} & J_{12}J_{23} - J_{22}J_{13} \\[2mm] J_{31}J_{23} - J_{21}J_{33} & J_{11}J_{33} - J_{13}J_{31} & J_{21}J_{13} - J_{11}J_{23} \\[2mm] J_{21}J_{32} - J_{31}J_{22} & J_{31}J_{12} - J_{11}J_{32} & J_{11}J_{22} - J_{12}J_{21} \end{array} \right]
$$

$$\cdots \tag{A37}$$

Substituting Eq. A36 into Eq. A28 gives the desired volume transformation for the hexahedron element. Equation A37 gives the explicit form of the inverse Jacobian matrix which is required in Eq. A34.

As mentioned in the previous section, a special evaluation of the bubble mode strain–displacement matrix (see Eq. A12) must be used in

order for the modified eight node hexahedron element to pass the patch test for an arbitrary element geometry. This modification involves evaluating the bubble mode shape function derivatives as (Taylor et al., 1976 and Cook, 1981)

$$
\left\{ \begin{array}{c} \dfrac{\partial N_j^b}{\partial x} \\[2ex] \dfrac{\partial N_j^b}{\partial y} \\[2ex] \dfrac{\partial N_j^b}{\partial z} \end{array} \right\} = \dfrac{|J_c|}{|J|} \; [J_c]^{-1} \left\{ \begin{array}{c} \dfrac{\partial N_j^b}{\partial \xi} \\[2ex] \dfrac{\partial N_j^b}{\partial \eta} \\[2ex] \dfrac{\partial N_j^b}{\partial \zeta} \end{array} \right\} \tag{A38}
$$

where $|J|$ is the Jacobian determinant of Eq. A36, $|J_c|$ is the Jacobian determinant evaluated at the element centroid (i.e. $|J_c| = |J(\xi=\eta=\zeta=0)|$) and $[J_c]^{-1}$ is the inverse Jacobian matrix of Eq. A37 evaluated at the element centroid. With the modification of Eq. A38 the modified eight node hexahedron element passes the patch test. Consequently, this element converges to the correct equilibrium solution with increasing mesh refinement.

With the curvilinear coordinate transformations presented in this section, the isoparametric finite element equations can be generated. Unfortunately, due to the algebraic complexity of the transformations, closed form evaluation of the element integrals is generally not possible. Evaluation of the element integrals is the topic of the next section.

Numerical Integration

Due to the complications introduced by isoparametric interpolation into the element stiffness matrix and load vector integrals, numerical integration (quadrature) must be used to evaluate the integrals. Typically, in finite element applications, Gaussian quadrature formulas are used due to their superior accuracy for a given number of quadrature point function evaluations. In the following paragraphs; line, surface and volume integral quadrature formulas are presented.

The line traction integral is represented as

$$
\int_{-1}^{1} [G^\ell(\xi)] \; J_\Gamma^\ell(\xi) \; d\xi \tag{A39}
$$

where $[G^{\ell}(\xi)] = [N^{\ell}]^T [N^{\ell}]$. Numerical evaluation of Eq. A39 is based on Gauss-Legendre quadrature which is represented as

$$\int_{-1}^{1} [G^{\ell}(\xi)] \, J_{\Gamma}^{\ell}(\xi) \, d\xi \quad \approx \quad \sum_{i=1}^{n^G} w_i \, [G^{\ell}(\xi_i)] \, J_{\Gamma}^{\ell}(\xi_i) \tag{A40}$$

where n^G is the number of Gauss-Legendre quadrature points, w_i is the ith weighting coefficient and ξ_i is the ith quadrature point. The value of n^G used in this report is two and the corresponding Gauss-Legendre data is given in Table A.1.

Evaluating the quadrilateral surface load integral and the element volume integrals is easily obtained by extending the one-dimensional integral of Eq. A40 into the second and third dimensions, respectively. Consequently, the surface load integral for the quadrilateral element becomes

$$\int_{-1}^{1} \int_{-1}^{1} [G^S(\xi,\eta)] \, J_{\Gamma}^S(\xi,\eta) \, d\xi \, d\eta$$

$$\sum_{i=1}^{n^G} \sum_{j=1}^{n^G} w_i \, w_j \, [G^S(\xi_i,\eta_j)] \, J_{\Gamma}^S(\xi_i,\eta_j) \tag{A41}$$

where $[G^S(\xi,\eta)] = [N^S]^T [N^S]$ and the volume integral for the modified hexahedron and infinite elements becomes

$$\int_{-1}^{1} \int_{-1}^{1} \int_{-1}^{1} [G^V(\xi,\eta,\zeta)] \, |J(\xi,\eta,\zeta)| \, d\xi \, d\eta \, d\zeta$$

$$\sum_{i=1}^{n^G} \sum_{j=1}^{n^G} \sum_{k=1}^{n^G} w_i \, w_j \, w_k \, [G^V(\xi_i,\eta_j,\zeta_k)] \, |J(\xi_i,\eta_j,\zeta_k)| \tag{A42}$$

in which $[G^V(\xi,\eta,\zeta)] = [B]^T [C_{ep}] [B]$. The global derivatives of the N_i shape functions used in the element strain-displacement matrices (Eqs. A12 and A25) are calculated using the transformation of Eq. A34 whereas the bubble mode shape function derivatives are obtained using the transformation of Eq. A38.

Stress and Strain Calculations

The soil elasticity constitutive relationships which are used to construct the elastic constitutive matrix, $[C_E]$, require an accurate determination of the effective stresses $\{\sigma'\} = \lfloor \sigma'_{xx} \ \sigma'_{yy} \ \sigma'_{zz} \ \tau_{xy} \ \tau_{yz} \ \tau_{zx} \rfloor^T$. Displacement based finite element analyses typically result in accurate displacement approximations but much less accurate stress representations. Barlow (1976) investigated the existence as well as a method of locating optimal points for calculating accurate stresses for displacement based finite element formulations. His technique involves subjecting the finite element to a complete polynomial field of one order higher than the complete polynomial representation included in the shape function approximation. The objective being to locate unique positions within the element at which the stresses have the same degree of accuracy as the nodal displacements. Hence, the terminology "optimum stress locations."

Barlow (1976) found that the optimum stress point is the element centroid (i.e. $\xi=\eta=\zeta=0$) for the eight node hexahedron. Numerical experimentation by the authors has verified that the centroid is also an optimum location for the modified eight node hexahedron element. Consequently, the element strains and stresses used to generate the elasto-plastic constitutive matrix are based on the element centroid for both the modified eight node hexahedron element (Fig. 5c) and the eight node isoparametric infinite element (Fig. 5d). Extenting the centroid stress evaluation concept to the infinite element is based on the fact that its shape function representation is a complete linear polynomial in terms of ξ, η and ζ.

When evaluating the modified hexahedron element stresses at arbritrary points, the bubble mode displacement parameters must be known in order to define the element strains (see Eq. A12). Recovery of the element bubble mode parameters are obtained from Eq. A15 once the incremental displacements have been generated from the nonlinear solution procedure. However, since $\lfloor B^B(\xi=\eta=\zeta=0) \rfloor$ is identically zero, no recovery of the bubble mode displacements is required (Hughes, 1987). Thus, the element incremental strains are evaluated as

$$\{d\epsilon\} = [B^H(\xi=\eta=\zeta=0)] \ \{dp^e\} \qquad (A43)$$

for the modified eight node hexahedron element and

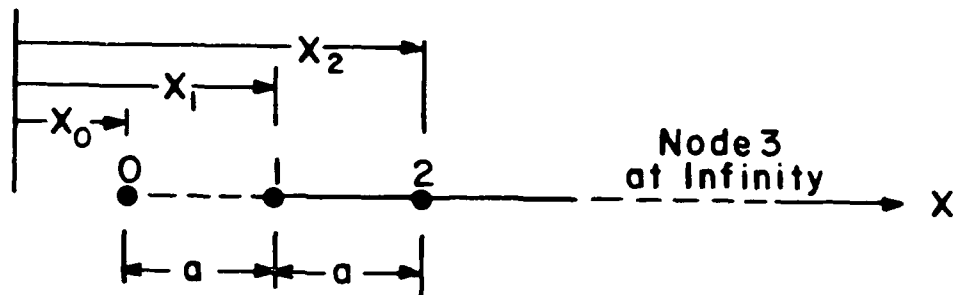$$\{d\epsilon\} = [B(\xi = \eta = \zeta = 0)] \{dp^e\} \tag{A44}$$

for the isoparametric eight node infinite element. Element incremental effective stresses are also evaluated at the centroid as
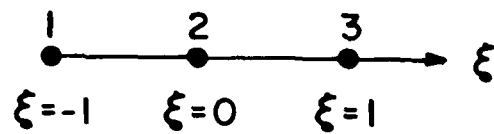
$$\{d\sigma'\} = [C_E] \{d\epsilon\} \tag{A45}$$

where $[C_E]$ and $\{d\epsilon\}$ are both evaluated at the element centroid.

Table A.1 Two Point Gauss-Legendre Quadrature Data

i	ξ_i	w_i
1	-0.57735 02691 89626	1.00000 00000 00000
2	0.57735 02691 89626	1.00000 00000 00000

(a) Global Representation

(b) Local Representation

Fig. A.1. One-Dimensional Infinite Finite Element

17